LUND UNIVERSITY

ON THE WAKE STRUCTURES OF FLOW AROUND DEFORMING AND VIBRATING BODIES

Cesur, Alper

2013

Link to publication

Citation for published version (APA):
Cesur, A. (2013). *ON THE WAKE STRUCTURES OF FLOW AROUND DEFORMING AND VIBRATING BODIES*. [Doctoral Thesis (compilation), Fluid Mechanics].

Total number of authors:
1

General rights
Unless other specific re-use rights are stated the following general rights apply:
Copyright and moral rights for the publications made accessible in the public portal are retained by the authors and/or other copyright owners and it is a condition of accessing publications that users recognise and abide by the legal requirements associated with these rights.
• Users may download and print one copy of any publication from the public portal for the purpose of private study or research.
• You may not further distribute the material or use it for any profit-making activity or commercial gain
• You may freely distribute the URL identifying the publication in the public portal

Read more about Creative commons licenses: https://creativecommons.org/licenses/

Take down policy
If you believe that this document breaches copyright please contact us providing details, and we will remove access to the work immediately and investigate your claim.

LUND UNIVERSITY

PO Box 117
221 00 Lund
+46 46-222 00 00

ON THE WAKE STRUCTURES OF FLOW AROUND DEFORMING AND VIBRATING BODIES

Doctoral Thesis

Alper Cesur

Division of Fluid Mechanics
Department of Energy Sciences

Lund, Sweden, 2013

LUNDS UNIVERSITET

Thesis for the degree of Doctor of Philosophy in Engineering.
ISBN 978-91-7473-555-0 (Tryckt)
ISBN 978-91-7473-556-7 (PDF)
ISSN 0282-1990
ISRN LUTMDN/TMHP-13/1093-SE

©Alper Cesur, May 2013
Department of Energy Sciences, Division of Fluid Mechanics
Faculty of Engineering
Lund University
Box18
SE-221 00 LUND
Sweden

Typeset in LaTeX
Printed by Media-Tryck, Lund, May 2013.

Populärvetenskaplig Sammanfattning

Datorsimuleringar, konsten att modellera verkliga eller tänkta händelser med hjälp av en dator och ett lämpligt simuleringsprogram, har blivit ett dominerande verktyg inom tekniska och naturvetenskapliga områden, likväl inom akademiska och industriella tillämpningar. Trots att experimentella studier har ett vedertaget erkännande inom diverse forskningsstudier har den snabba utvecklingen av datorprestanda, mjukvara och algoritmer gjort att datorsimulering blivit ett vitalt och väletablerat komplement till kostsamma experiment.

Vid bruk av datorsimularingar utgår man från en matematisk modell för att beskriva ett fysikaliskt förlopp för att i sin tur kunna studera det fenomen som man är intresserad av. Därefter används varianter av beräkningsmetoder för att kunna genomföra simuleringarna.

Fenomenet Fluid-Struktur Interaktion, vilket är forskningsämnet, existerar i en rad tillämpningsområden i praktiken. Luftpartiklars strömning kring en flexibel flygplansvinge eller hängbro samt vattenpartiklars passage kring havsplattformar och/eller propellrar till havsfartyg är några utav många exempel där en direkt/indirekt interaktion mellan föremålen i fråga och mediet i sig kan klassificeras under kategorin Fluid-Struktur Interaktion; FSI. Denna interaktion (mellan fluid och struktur) kan under stränga förhållanden leda till oönskade händelser såsom falering av en flygplansvinge, kollaps av en bro samt/eller häftiga vibrationer av t.ex. borrnings-rör som är fast förankrade till oljeplattformar.

Syftet med denna forskningsstudie är att kunna reda ut och prediktera de fysikaliska mekanismer som ligger till grund och kan ge upphov till ovan nämnda oangelägenheter. Detta har undersökts genom att studera hur karaktären på rörelsen och/eller deformationen hos strukturen förhåller sig till dynamiken i dess vak, vilken representeras av kvantiteter som flödeshastighet och tryck. Målet är bland annat att på en erforderlig nivå kunna beskriva och förklara kopplingen mellan varierande fasförhållanden som typiskt karaktäriserar dynamiken hos strukturen och dess korresponderande (tidsberoende) vak.

Dessa mål ställer dock höga krav på precission och effektivitet hos tillgängliga beräkningsmetoder samt de metoder som är under utveckling. I synnerhet behöver metoderna kunna hantera väldigt stora system

på grund av höga krav på upplösning i simuleringarna och dessutom behöver de ha någon form av felkontroll för att säkerställa noggrannheten i simuleringarna.

I denna avhandling har två objekt av olika geometri och uppsättning använts för att studera interaktionen mellan fluid och struktur, nämligen en elastiskt upphängd stel cirkulär cylinder och en flexibel rektangulär balk med ett kvadratiskt tvärsnitt som är fast inspänd i den ena änden och fri i den andra. Den stela cirkulära cylindern har brukats i ett renodlat studiesyfte och resultaten har analyserats med utgångspunkt från tidigare utförda studier. Arbetet för den fast inspända balken, å andra sidan, omfattade dels utveckling av en beräkningseffektiv metod, genom att fördela beräkningsarbetet jämbördigt i delproblem mellan flertal datorer, och dels en studie kring metodens styrka och dess begränsningar.

Abstract

This thesis concerns the study of Fluid-Structure interaction phenomena among deforming and (non-deforming) vibrating objects under unsteady fluid flow exposures. This multi-physical phenomenon is widely encountered in real-life situations and therefore it is of significant importance to understand the underlying physics. The trend is that both industrial and research facilities aim for developing methods that treat this complex and multi-disciplinary problem with high accuracy and also sufficient efficiency.

Time-domain simulations, that is the dominating prediction tool within the FSI-community although frequency-domain representation is still used to some extent, have been integrated with two different structural models that model the solid objects. For the vibrating rigid object an Immersed Boundary (IB) method based on the use of Cartesian mesh is used to represent the solid object by using momentum source that enforce the required boundary condition. The deforming object, on the other hand, is modelled by a three-dimensional Finite Element (FE) formulation based on collocated mesh formulation. An Arbitrary Lagrangian-Eulerian (ALE) formulation provides the deformation of the object which is solved in conjunction with the fluid and solid solvers. Further, a partitioned FSI-approach based on strong coupling strategy assures for reliable flow and solid domain quantities.

The time-dependent and unsteady fluid flow is predicted based on Implicit Large Eddy Simulations (ILES) which becomes a prerequisite in order to resolve flow processes involving large-scale structures with sufficient accuracy. In particular, separation processes, vortex shedding and possibly vortex-pairing are flow phenomena of such kind that typically are encountered when the flow around an object enforces the body to be deformed or displaced, which in turn, alters the character of the flow structures.

In the context of deformable- and rigid body motions, this study is especially focused in the near-wake (instantaneously) behaviour of flow structures in conjunction with dependency of wake topologies when the unsteady wake flow generates unsteady loading on the object. The variations in response dynamics of the objects are studied in parallel and

a direct/indirect coupling is made in the object-wake dynamics in order to better understand the complex two-way FSI phenomenon. In the analyses, particular post-processing tools for the fluid-flow, such as Proper Orthogonal Decomposition (POD) and Dynamic Mode Decomposition (DMD) have served as a toolbox. It is shown that very useful conclusions can be drawn and hence, attribute these findings to relevant mechanisms underlying the FSI problem.

List of Papers

This thesis is based on the following papers, which will be referenced by CAPITAL letters in the body text of the thesis. The papers are appended in the order listed below.

I A. Feymark, **A. Cesur**, N. Alin, C. Fureby, J. Revstedt, R. Bensow. "Fluid-Structure Interaction using Parallel Open Source Software with Application in Hydroelasticity". *Submitted to Journal of Computational Physics, 2013.*

II **A. Cesur**, A. Feymark, J. Revstedt. "A Large Eddy Simulation Based Fluid-Structure Interaction Study of a Stiff and a Flexible Cantilever Beam". *Submitted to Journal of Physics of Fluids, 2013.*

III **A. Cesur**, C. Carlsson, A. Feymark, L. Fuchs, J. Revstedt. "Analysis of the Wake Dynamics of Stiff and Flexible Cantilever Beams using POD and DMD". *Submitted to Journal of Computers & Fluids, 2013.*

IV **A. Cesur**, C. Carlsson, L. Fuchs, J. Revstedt. "Modal Analysis for Oscillating Cylinder Arrays at Low Reynolds number". *Submitted to Journal of Fluids and Structures, 2013.*

Other Related Work by the Author

A. Cesur and J. Revstedt. "Vortex Induced Vibrations of Multiple Cylinders". *P*roceedings of the Twenty Second Nordic Seminar on Computational Mechanics, 2009.

A. Cesur and J. Revstedt. "Influence of Staggering on Wake Dynamics of Multiple Cylinders". *I*UTAM Symposium on Bluff Body Wakes and Vortex-Induced Vibrations (BBVIV-6), 2010.

A. Feymark, **A. Cesur**. "Fluid-Structure Interaction Using Open Source Software". *P*roceedings of the 14th Numerical Towing Tank Symposium, 2012.

Acknowledgement

This project was sponsored by the Swedish Research Council (VR) and the work was carried out at the Division of Fluid Mechanics, Faculty of Engineering at Lund University (Sweden). The computations were run at the Swedish National Infrastructure for Computing (SNIC) in the Center for Scientific and Technical Computing for Research at Lund University, LUNARC.

First of all, I would like to acknowledge my supervisor, Prof. Johan Revstedt, for giving me the opportunity to join the world of science. Although it sometimes was 'easy' and sometimes quite painful, to not mention the many many sleepless nights, I would like to thank you for always, in a constructive manner, pushing me towards the furthest edge. It has brought me to an other level.

I would also like to thank Prof. Laszlo Fuchs for his encouragements during this project. Further, Prof. Xue-Song Bai, thank you for keeping the 'flame' alive regarding the social network within the group of Fluid Mechanics at Lund University. Dr. Robert Szasz, great thanks for always considering my complaints on the printer and for fixing my computer-needs within less than five minutes!

I would also like to thank Prof. Christer Fureby and Nicklas Alin at FOI (Swedish defence research agency) and Prof. Rickard Bensow at Chalmers University for valuable discussions and collaborations.

A particular side note for Andreas Feymark at Chalmers University and Christian Carlsson at Lund University. In academical terms, thanks for being the 'inflection point' in my scientific life-time! In particular, many thanks for your sincere and valuable discussions, sometimes reaching into midnights!

I am also grateful that I met and became familiar with PhD students at the division of Fluid Mechanics. 'Große' thanks to Holger for proof reading my thesis carefully. In addition; Holger, wieder danke für deine andere Übersetzung! Erdzan, I would like to thank you as well for giving a try! Naser, great thanks for your support to my thesis with your 'extremely' advanced CAD programme. Ali-Alsam and Rickard thanks for being the positive mechanisms of happiness in the division of Fluid Mechanics. Mohammed, thanks for your contribution with your ideas

and skills in the experiments! For the rest; Aurélia, Hessam, Henning, Cheng, Yajing, Jiangfei, Vivianne, Fan, Rixin, Mehdi, Emma. I also want to express my sincere gratitudes to all of you.

Lastly, Mother and Father; the two persons being the underlying reason for all my happiness and success in life, I want to thank you DEEPLY for your unconditional support!!! I also want to send my gratitudes to two princesses, my sisters, for their spiritual support during my PhD time.

Contents

1 Introduction **1**

2 Physics of FSI **5**
2.1 Flow Past Stationary Bluff Bodies 5
2.2 Elastically Mounted Circular Cylinders 11
2.2.1 Vortex Induced Vibrations 11
2.2.2 Forced Cylinder Oscillations 21
2.3 FSI on Flexible Cantilever 27

3 Fluid Motion **31**
3.1 Governing Equations for Fluid Dynamics 31
3.1.1 Fixed Mesh 32
3.1.2 Deforming Mesh 33
3.2 Numerical Methods and their Discretizations 34
3.2.1 Finite Differences and Staggered Grid Formulation 35
3.2.2 Finite Volumes and Collocated Grid Formulation . 39

4 Turbulent Flows **43**
4.1 Phenomenological Description 43
4.2 Large Eddy Simulation 46

5 Solid Body Motion **51**
5.1 Theory of Solids and their Deformation 51
5.1.1 Total Lagrangian Formulation 52
5.1.2 Constitutive Relationship and Element Formulation 53
5.2 Numerical Treatment of Solids 55
5.2.1 Non-linear Finite Element Formulation 55

6 Two-way FSI Methodology **61**
6.1 Interface Treatment and Flexible Cantilever 61
6.1.1 Explicit Coupling 64
6.1.2 Implicit Coupling Strategy 66
6.2 Moving Boundaries and Rigid Cylinder 69
6.2.1 Boundary Conditions 71

7 Post-processing Tools **77**
7.1 Proper Orthogonal Decomposition (POD) 77
7.2 Dynamic Mode Decomposition (DMD) 80

8 Unpublished Work **83**

9 Concluding Remarks **89**

10 Summary of Publications **91**

List of Figures

2.1 Bluff bodies with increasing degree of bluffness-es from top to bottom. 6

2.2 Strouhal number - Reynolds number dependency for a circular cylinder. From Roshko [1] and Norberg [2]. 10

2.3 A schematics of the elastically mounted circular cylinder. 11

2.4 Two distinct types of amplitude response are shown schematically. High-($m^\star\zeta$) parameter results in only two branches (initial and lower) while low-($m^\star\zeta$) type of response exhibits three response branches (initial, upper and lower). The range of $V^\star$ for synchronization is controlled primarily by $m^\star$ (when ($m^\star\zeta$) is constant), whereas the peak amplitudes are controlled principally by the product ($m^\star\zeta$). . . 14

2.5 Response amplitude (a) and frequency (b) for an elastically mounted rigid cylinder. Symbols; ■: $m^\star = 2.4$ and $\zeta = 0.0045$ Khalak and Williamson [3] experimental data, ▲: $m^\star = 248$ Feng [4] experimental data, •: $m^\star = 2.7$ Cesur [5] numerical simulations. From Khalak and Williamson [3] with the addition of data from Cesur [5]. 16

2.6 The set of vortex wake modes for a cylindrical structure. The $2C$ mode is found for the vibration of a pivoted cylinder (Flemming and Williamson [6]). 20
2.7 Schematic diagrams illustrating the behaviour of the total and vortex phases for (a) the free response branches at low-$m^\star\zeta$ values and (b) the corresponding forced wake states at a high $A^\star$, whereas (c) shows the amplitude response of the low-$(m^\star\zeta)$ type showing the principal branches, and correspondingly the jump phenomena. 25
2.8 A comparison between amplitude response, $A^\star$, for a flexible cantilever and an elastically mounted rigid cylinder, as a function of normalized velocity, $V^\star$. Symbols; ○: Pesce and Fujara [7] data, ■: Khalak and Williamson [8] data, ⋆: Revstedt [9] data. From Fujarra et al. [10] and Revstedt [9]. 29

3.1 Two-dimensional staggered finite-difference grid. 37
3.2 Face Interpolation scheme. 41

4.1 Energy spectrum of turbulent flow, $E(k)$, as a function wave number, k. 44

5.1 Linear tetrahedral element, definition and node numbering. 54

6.1 Fluid-structure interaction problem subdivided into fluid and solid domains with inherent boundaries. 62
6.2 Sketches for realizations of three interface treatment prototypes. Left; DFMT, Middle; Mortar, Right; LLM. . . . 63
6.3 Conventional sequential staggered (CSS) approach. 65
6.4 Partitioned approach for implicitly coupled FSI with relaxation technique. 68
6.5 A schematics of the Immersed Boundary mesh crossing the fluid mesh. 73

8.1 A schematics of the experimental arrangement. 84
8.2 Pictures of the cylinder assembling in the test-section. . . 85
8.3 Image processing and detection procedure. 86

8.4 Amplitude and frequency response of the transversal cylinder motion from experiments for $m^{\star}$=1.35. 88

CHAPTER 1

Introduction

Since the start of the scientific revolution a specific interest in fluid motion has emerged as a vital subject on its own, which can be traced back to the early 16th century. In the modern world, a particular branch has evolved under fluid mechanics which describes details of fluids and the forces on them. A similar trend can be drawn for solid materials which are characterized by structural rigidity and resistance to changes of shape or volume and falls under the branch solid mechanics. Civil (and structural)- and mechanical engineering, geology and material science are disciplines that study the behaviour of solid materials, particularly their motion and deformation under the action of forces and other external or internal parameters. The parallel disciplines for fluids involve e.g. chemical engineering, aerospace engineering, medical engineering and, also, material sciences. It is a field where *multiple* physical effects can be met, for example the motion of a fluid flow and the deformation or displacement of a structure and their mutual interaction. Fluid-Structure Interaction (FSI) is the name of such a dynamic (or in some cases a static) state of an object, e.g. a structure, where external (or internal) fluid forces act on it so as to alter the structural response, which in return, affects the surrounding (or embracing) fluid flow.

General examples of FSI problems in engineering fields and applied sciences are flows around elastic structures, e.g. aeroplanes and submarines, categorized under aero- and hydroelasticity, respectively and flows in elastic structures, e.g. haemodynamics, i.e. the transport of blood in aortas. Research facilities on such FSI applications (and other types as well) comprise, from a historical point of view, mostly experimental studies. Nevertheless, the ongoing development of computational software and resources in either of the inherent FSI branches have made numerical simulations of these problems a robust and reliable candidate for experiments.

Numerical predictions of FSI problems of deformable objects are performed using Computational Fluid Dynamics (CFD) and Computational Structural Dynamics (CSD) solvers as a coupled system. In the literature there exist two distinct coupling approaches for this purpose, namely the monolithic and partitioned approaches. In the monolithic approach the fluid- and solid system of equations are solved for simultaneously, including the boundary conditions. In the partitioned approach, on the other hand, the governing equations for either of the fields are solved as separate subsystems in a staggered manner, where a coupling is required as an additional coupling interface. Here, aspects such as solver-to-solver communication and/or grid-to-grid interpolations have to be considered.

The partitioned schemes are further subdivided into explicit and implicit coupling schemes. Explicit coupling schemes solve the fluid and solid equations without any sub-iteration, leading to severe stability problems in most applications. These schemes are generally favoured in aeroelastic applications [11], where the difference in density between fluid and solid is typically large. To overcome the stability problem arising from the partitioning and to enforce the continuity coupling condition, implicit coupling schemes are utilized. For the implicit coupling schemes the fluid and structure solutions are repeated until certain convergence tolerance is reached. Normally, this is a procedure which involves finding equilibrium between large systems of non-linear equations using iterative solvers, e.g. block-Jacobi, block-Gauss-Seidel or relaxation methods such as Aitken's relaxation method. Applications of implicit schemes, where the fluid and solid densities are of comparable order, can for instance be found in biomedicine [12] and hydroelasticity [13].

Normally, any structure immersed into a cross-flow, for instance a cylinder representing the pillar of offshore structure or mooring cable, will be subjected to unsteady lift forces due to the asymmetric shedding of vortices from the upper/lower surfaces of the structure. Under certain conditions, i.e. when the frequency of the shed vortices and also the frequencies of the structure's motion coincide or more correctly locks onto the natural frequency of the structure, extremely high vibrations may commence. 'Locked-on' states is an accepted terminology within the more general designation of Flow-Induced Vibrations (FIV) or the more specific Vortex-Induced Vibrations (VIV) that features a feedback process of high energy transfer in-between the two agents of fluid-flow and structure. In particular, the three-dimensional repetitive pattern of flow (or vortex-wake) structures developing in the near-wake of the structure play an important role in the overall fluid-structure interaction process. By nature, these locked-on states are (most often) highly unwanted and therefore the main objectives becomes to reduce them or at least control and outline the underlying mechanisms. For this reason, a better understanding and predictions of flow induced vibrations might prevent fatigue and/or failure of bridges, buildings, aeroplane wings, etc. Other flow-induced related issues concern for instance the production of noise which typically occurs at rotating devices such as propellers and/or turbine blades. In this case, reducing the noise levels become important from the perspective of human comforts.

Purpose and Objectives

The main purpose of this thesis work is to improve the understandings of the physics of the interaction between unsteady fluid flows and structure(s) with specified size, shape and material properties. Numerical simulations are carried out within the large eddy simulation framework, which is a high fidelity approach that provides detailed information at the various length and time-scales.

The objectives, in accordance with the purpose of the work, are as follows:

- Analysis and understanding of the physics of the flow around a

single and multiple rigid cylinders. Both frequency locking- and non-locking effects are considered.

- Determine the interaction between the flow and several rigid, elastically mounted structures, moving relative to each other at some parameter ranges for different geometrical configurations.
- Carry over the analysis for rigid circular cylinders to encompass flexibility effects, i.e. deformation, of a cantilever beam and its interaction with wake instabilities.
- Characterize the possible physical mechanisms of the fluid-structure interaction phenomena between single and multiple cylinders, and also between a stiff and flexible cantilever beam.

For the achievements of the first two bullets two different decomposition techniques were used, Proper Orthogonal Decomposition (POD) and Dynamic Mode Decompositions (DMD).

For the second last bullets, on the other hand, code development was required in order to facilitate the simulations for objects with body flexibility. Within this scope, particular effort was made in the developing of a functional structural solver in the open source program OOFEM [14, 15]. At the start of the project no implicit dynamical solver was available in OOFEM, which was a prerequisite for the planned application area in this thesis work and not least for future applications, such as haemodynamics.

CHAPTER 2

Physics of FSI

2.1 Flow Past Stationary Bluff Bodies

The importance of predicting the influence of viscosity on the behaviour of a fluid in a particular set of circumstances plays a major role when characterizing different flow regimes in a fluid flow. For 'external' flows around bodies immersed in a fluid stream, viscous effects might be of considerable level near the body surfaces and in its near-wake. Depending on the body shape and flow properties different flow regimes may be identified and this will be discussed in more detail below.

These flow regimes, called *laminar* and *turbulent*, are characterized by the Reynolds number, Re, which was introduced in 1883 by Reynolds [16]. The Reynolds number quantifies the relative importance between the ratio of inertial and viscous forces as

$$Re = \frac{VL}{\nu} = \frac{\text{Inertial forces}}{\text{Viscous forces}}, \tag{2.1}$$

where V is a characteristic velocity of flow, L is a characteristic length and ν is kinematic viscosity of the fluid. Hence, low Reynolds number corresponds to viscous forces dominating whereas high Reynolds number corresponds to viscous forces being negligible compared to inertial forces.

Viscosity effects, large region of separated (external) flow, a high value of drag coefficients and the classical phenomenon of vortex shedding are features of the flow field that characterize a 'bluff body' within the context of fluid mechanics. Figure 2.1 shows three kinds of bluff bodies with varying bluffness-es. The 'degree of bluffness' for a rigid body exposed to external flow field is referred to as the ratio between the cross-flow dimension of the separated wake and the extent of the body surface immersed in the separated wake. With respect to this definition, the airfoil geometry (Figure 2.1 (a)) is regarded as a streamline body due to its small wake and the rectangular flat plate normal to the free-stream (Figure 2.1 (c)) is regarded as the body with maximum bluffness.

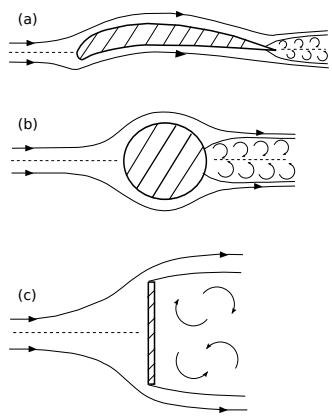

Figure 2.1: Bluff bodies with increasing degree of bluffness-es from top to bottom.

Depending on flow regime, the flow around a bluff body will exhibit a certain periodic buildup and subsequent shedding of vortices, which in a non-dimensional form in terms of a Strouhal number, St, is expressed as (introduced by Strouhal [17])

$$St = \frac{f_s L}{V}, \tag{2.2}$$

where f_s is a vortex-shedding frequency, V is the characteristic velocity of flow and L is the characteristic length scale. It is an important flow parameter which represents the relation between transient and convective terms to describe oscillating flow mechanisms.

Historically, different models have been developed in order to qualitatively describe the flow around an arbitrary bluff body. With the aim of establishing universal laws for the the essential mechanism underlying for the cause of e.g. high drag and lift, several methods describing the relationship between the wake and the body of consideration have been reported. In the early 1950s, Roshko [18] made an experimental study of the flow around two-dimensional bodies of varying bluffness-es; a circular cylinder, a 90° wedge and a 'flat plate' positioned normal to the flow. The investigation was aimed at finding a relation between the flow characteristics in the immediate vicinity of the cylinders and at the wake further downstream, with the hope of finding a solution dependent on only one experimental measurement. A dimensional analysis of an analytical model of the near-wake region gave a universal Strouhal number, $St^\star$, which was then experimentally determined as a function of wake Reynolds number, $Re^\star$. This result, together with free-streamline theory, allowed the drag to be calculated from a measurement of the shedding frequency and furnished a useful correlation between different bluff bodies. Moreover, by allowing for some annihilation of the vorticity in the free shear layers, it was shown how to combine the Kirchhoff [19] solution, attributed to the free-streamline theory, and the von Kármán vortex street [20]. The conclusions from this work was that additional (empirical) relation is needed for more understanding of the flow in the region of vortex formation.

Bearman [21] made an extensive research on fixed and oscillating bluff bodies, in which he discusses the importance of the mechanism of the production of vortex shedding. He reports among else the opening research performed by Gerrard [22] on the mutual interaction between two separating shear layers which is considered as a key factor in the formation of a vortex-street wake. Here, properties of the flow such as circulation, oppositely signed vorticity and entrainment are significant for the vortex-formation model. An other approach (for the vortex-formation model) may be to estimate the rate of shedding of circulation from a bluff body

by considering the mean base pressure, as in [23, 18]. To shine some light in to the understanding of vortex shedding phenomenon Abernathy and Kronauer [24] were able to show, from their numerical simulations, that it is the presence of two shear layers, rather than the bluff body itself, that is principally responsible for vortex shedding.

Flow Past Rigid Cylinders

The circular cylinder has for a long time been accepted as the canonical geometry for two-dimensional bluff bodies. This (postulated) generic nature of the circular cylinder was strengthened when Roshko [18] formulated the Universal Strouhal number, $St^\star = (St\, d')/(k^\star\, d)$, where S is the usual cylinder Strouhal number, $k^\star$ is a parameter depending on the base pressure, d is the dimension related to the body whereas d' represents the wake width (as a function of $k^\star$). The important result for this consideration is actually that a wake width (d') is defined, where $St^\star$ collapses the two-dimensional wake structure of different short bodies with respect to the vortex shedding frequency and base pressure. Among others, Roshko [18], Bearman [25, 26] and Narasimhamurthy and Anderson [27] clarify the coupling between the base pressure and the evolution of various two- and three-dimensional wake instabilities as the Reynolds numbers are varied. Especially, the sensitive response of the base pressure is reported with respect to the process of vortex formation in the near wake by plotting the base suction coefficient $-C_{Pb}$ versus the Reynolds number. Narasimhamurthy and Anderson [27] note that a reduction in base pressure is associated with a stronger vortex formation due to a shorter recirculation length and an increase in St.

The variability of the separation-point for a circular cylinder further adds to the complexity of the problem, which is pronounced implicitly at the determination of the 'critical' Reynolds number of bluff body flows. As the Reynolds number is increased the flow undergoes tremendous changes with respect to the two flow regions, namely the boundary layer and the wake. The latter is composed by regimes of vortex shedding which occurs due to instabilities in the flow and can be described as follows; Initially, the transition scenario from a steady wake flow field to laminar two-dimensional von Kármán shedding, indicated by a Hopf

bifurcation instability, occurs at $Re \approx 47$, which has been outlined by for example Dusek et al. [28]. Further transition results in the formation of three-dimensional vortex structures in the wake when the Reynolds number exceeds a critical value of $Re \approx 190$. As the Reynolds number is increased through the critical value Williamson [29] reports that the character of the wake of the flow is composed of interrelated properties of two instability modes. These are referred to as *Mode A* and *Mode B* shedding with spanwise wavelengths of $3 - 4$ and approximately 1 cylinder diameter, respectively. The critical Reynolds number for Mode A transition, which exhibits out of phase symmetry, was observed by Miller and Williamson [30] to occur at $Re = 194$. The transition of Mode B instability, exhibiting in phase symmetry, was observed in the range of $230 \leq Re \leq 250$ by Williamson [29]. The interrelated effect between Reynolds number and Strouhal number deserves a particular observance. Roshko [1] and Norberg [2] both quantified the vortex street behind a circular cylinder where the non-dimensional vortex shedding frequency has been investigated with respect to Reynolds number, as can be seen in Figure 2.2. Here, Roshko gives expressions for the Strouhal number as function of the Reynolds number individually for the low- and high Reynolds number range based on experimental data. He also discusses three different ranges in terms of Reynolds number; the stable range from $40 \leq Re \leq 150$, the transition range from $150 \leq Re \leq 300$ and the irregular range above $Re = 300$. Nevertheless, it is of course of interest to investigate whether the transition sequence found for circular cylinders is also valid for other bluff bodies. Does the results obtained for the circular cylinder wake describe all important three-dimensional instability modes observed for nominally two-dimensional cylindrical bodies of different geometries, i.e. is the wake transition scenario observed for a circular cylinder effectively the generic scenario for all bluff bodies? Ryan et al. [31] investigated the transition scenario to three-dimensional wake, i.e. the behaviour and character of Mode A and Mode B instability. This was done for an elongated cylinder (or plate) with an aerodynamic leading edge and square trailing edge. The three-dimensional instability modes were determined as a function of the chord to thickness ratio (aspect ratio). The conclusions was that an increase in the aspect ratio alters the

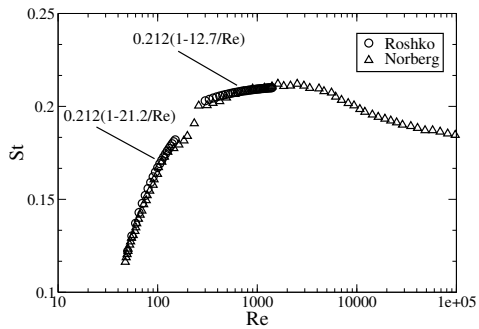

Figure 2.2: Strouhal number - Reynolds number dependency for a circular cylinder. From Roshko [1] and Norberg [2].

preferred mode of instability. However, for very short bodies, Mode A is the dominant one and it is expected that the transition scenario be similar to that of a circular cylinder. For intermediate aspect ratio bodies, i.e. for $AR_1 > 7.5$, Mode B′ (with the same spatio-temporal symmetry of Mode B for a circular cylinder but a much longer wavelength) becomes the initial mode of instability in preference to Mode A, where the critical Reynolds number is approximately $Re = 450$. For very long aspect ratio bodies $AR_1 > 17.5$, the outcome may result in Mode A not becoming critical at all due to the development of Mode B.

Following Schewe [32] the boundary layer over the cylinder surface remains laminar over the range $300 < Re < 3 \times 10^5$, which is called the subcritical flow regime. With a further increase in Reynolds number a transition into turbulence occurs in the boundary layer itself where the region of transition moves upstream over the cylinder surface towards the stagnation point. Initially, in the region of $3.0 \times 10^5 < Re < 3.5 \times 10^5$, the boundary layer is turbulent at one side and laminar at the other side causing asymmetric flow over the cylinder. This flow regime is called the critical flow regime. The next Reynolds number regime is the so called supercritical flow regime where $3.5 \times 10^5 < Re < 1.5 \times 10^6$, at which the boundary layer separation is turbulent on both sides of the cylinder, however no yet complete. Finally, in the transcritical flow regime, $Re >$

4.5×10^6, the boundary layer over the cylinder surface is fully turbulent everywhere.

2.2 Elastically Mounted Circular Cylinders

In the previous sections the main features of the laminar flow past a stationary bluff body, such as flat plate normal to free-stream and circular cylinder, have been discussed. In many applications, though, the body of consideration is not fixed but oscillates at a given frequency that may interact with the vortex shedding process at the wake and thus alter its structure. In this thesis, the transversal oscillations of an elastically mounted circular cylinder forms principally the major concern among vortex-induced vibrations systems, and indeed works as a prototype for; forced structure oscillations; structures in two degrees of freedom; flexible structures, to name a few.

2.2.1 Vortex Induced Vibrations

Vortex induced vibrations (VIV) are motions induced on bluff bodies interacting with an external fluid flow, where these motions are produced by certain periodical irregularities in the wake of the body. In contrast to forced cylinder oscillations the frequency and amplitude of the cylinder motion is not known *a priori*.

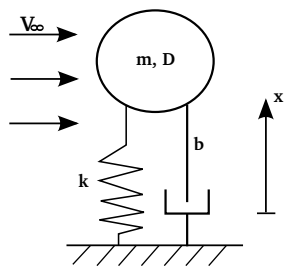

Figure 2.3: A schematics of the elastically mounted circular cylinder.

An elastically supported circular cylinder is regarded as the simplest case in the general subject of bluff body-fluid structure interactions. The

two-dimensional cylinder system, allowed to vibrate only transverse to the free-stream is presented in Figure 2.3 and described by the following structural parameters: mass m, damping b, spring constant k and cylinder diameter D. The fluid parameters are the fluid density ρ, kinematic viscosity ν and free-stream velocity V_∞. One of the important parameters related to oscillating structures is the natural frequency of the structure, defined as $\omega_N = \sqrt{(k/m)}$.

Response Dynamics; Amplitude and Frequency of Motion for a Single Cylinder

In the context of various VIV systems (as mentioned above) the response of an elastically mounted cylinder is influenced by a set of non-dimensional parameters [33]; $m^\star$, ζ, $V^\star = V_\infty/(\omega_N D)$, $A^\star$, $f^\star$ and Re, which correspond to the non-dimensional mass, damping, (reduced) velocity, amplitude of oscillation, frequency of oscillation and the Reynolds number, respectively. One of the fundamental questions to be answered for various VIV systems has been to understand; how the maximum response amplitude depends on the system mass and damping? Generally, various relationships have been presented in the literature depending on the type of experiments conducted. Nevertheless the common approach has been to find a unique correlation between the response (peak) amplitude, $A^\star_{max}$, and, the product of the system mass and damping, $(m^\star\zeta)$. Among others, Vickery and Watkins [34], who considered an equation of motion for flexible cantilevers, plotted the peak amplitudes versus a 'stability parameter', K_s, defined as

$$\text{Stability parameter} = K_s = \pi^2(m^\star\zeta). \tag{2.3}$$

Furthermore, Scruton [35] used a parameter proportional to K_s for his experiments on elastically mounted cylinders, which has been termed the Scruton number [35]:

$$\text{Scruton number} = Sc = \frac{\pi}{2}(m^\star\zeta). \tag{2.4}$$

Skop and Griffin [36] compiled data from several different experiments to predict response amplitudes whereby they were able to derive a slightly

different parameter from the response analysis. The combined response parameter was subsequently termed S_G as:

$$\text{Skop-Griffin parameter} = S_G = 2\pi^3 St^2(m^\star\zeta). \tag{2.5}$$

Peak amplitudes, evaluated from the curve fits in the 'Griffin' plots under the limit of zero mass-damping from different physical experiments (such as, elastically mounted rigid cylinders exposed to one- and two degrees of freedom, cantilevers and pivoted cylinders, and forced cylinder oscillations) have shown that the largest attainable amplitudes lies between 0.8 and 1.6 according to Williamson and Govardhan [37]. Here, they present an extension of the log-log Griffin plot for a variety of experiments compiled by Skop and Balasubramanian [38] but, plotted with a linear Y- axis. From the various experiments, a large scatter of the data was observed and the conclusion was that it seemed unreasonable to compile all the results into a single plot, with the hope that a single (unique) curve of data may ensue. This idea was strengthened by Sarpkaya [39], who stated that the response of the motion is governed by $m^\star$ and ζ independently, and *not* just by the combined mass-damping $(m^\star\zeta)$. Moreover, Zdravkovich [40] reports that a combined $(m^\star\zeta)$ parameter is not legitimate for $m^\star < 10$ in marine and offshore engineering whereas it is useful for wind engineering $m^\star > 100$. However, Williamson and Govardhan [37] presented later only those data consisting of uniformly similar set of experiments. Following the experimental work by Khalak and Williamson [33], which involves the transversal oscillations of an elastically mounted rigid cylinder, two distinct curves have been introduced into the Griffin plot representing the peak amplitudes for both the upper and the lower branches of the amplitude of the cylinder motion. The resulting data from the diverse experimental arrangements appear to give an approximate functional relationship between $A^\star_{max}$ and $((m^\star + C_A)\zeta)$ over a wide range of parameters. Here, C_A is the potential added mass coefficient taking the values 1.0 according to the potential flow theory.

To better understand the physical significance of the mass and damping ratios, the response dynamics of the cylinder amplitude of oscillations are (traditionally) plotted as a function of the reduced velocity, $V^\star$. In Figure 2.4, the contribution of each of these two parameters are schemat-

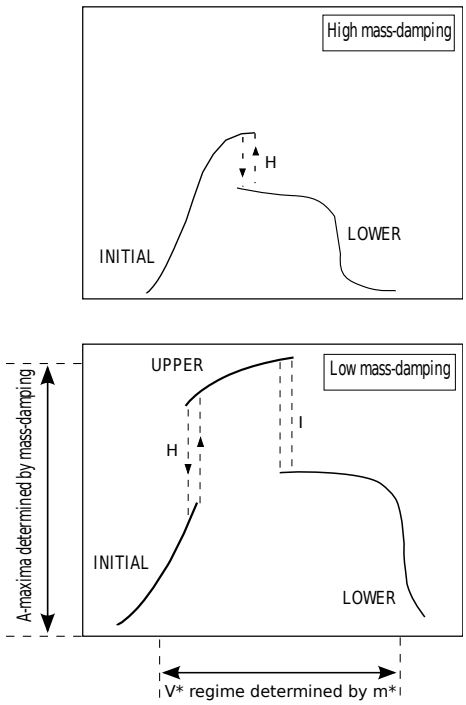

Figure 2.4: Two distinct types of amplitude response are shown schematically. High-$(m^\star\zeta)$ parameter results in only two branches (initial and lower) while low-$(m^\star\zeta)$ type of response exhibits three response branches (initial, upper and lower). The range of $V^\star$ for synchronization is controlled primarily by $m^\star$ (when $(m^\star\zeta)$ is constant), whereas the peak amplitudes are controlled principally by the product $(m^\star\zeta)$.

ically illustrated and the conclusions can be summarized as follows:

- the range of the *synchronization*, i.e. the range of $V^\star$ for which high amplitude of oscillations are achieved, is primarily controlled by mass ratio, $m^\star$, when $(m^\star\zeta)$ is constant.
- the peak amplitude of oscillations, on the other hand, are controlled principally by the product $(m^\star\zeta)$.

A study of Figure 2.4 puts a further the question; what modes of response exist as a function of mass and damping? This question is of vital interest in the ongoing research field of vortex-induced vibrations and acts as a template in the understanding of the physics within bluff bodies and VIV systems.

Khalak and Williamson [3] studied the amplitude and frequency response of a freely vibrating cylinder in water for $m^\star = 2.4$ and compared the results with those of Feng [4], who performed experiments in air with $m^\star = 248$. As it can be seen from Figure 2.5, the character of the amplitude response reveals other interesting VIV phenomena. For high $(m^\star\zeta)$, as in Feng [4], there are two different branches of amplitude response only, namely the 'initial' and 'lower' branch. In contrast to the high-$(m^\star\zeta)$ experiment by Feng [4], the low-$(m^\star\zeta)$ type of response by Khalak and Williamson [3] is characterized by three different branches of response. In addition to the 'initial' and 'lower' branches, they also find an 'upper' branch of response. The numerical simulations of Cesur [5] show a similar trend as those of Feng, although with a wider synchronization range, despite the low value of $m^\star$. This behaviour may be related to the low Reynolds number used for the simulations, $Re = 400$.

Moreover, Khalak and Williamson [3] have also shown that the transition between the Initial $\Leftrightarrow$ Upper branches is hysteretic, while the Upper $\Leftrightarrow$ Lower transition involves an intermittent switching.

The crucial engineering interest within bluff body dynamics exerted to external fluid flow has been to identify a clear definition for the synchronization or lock-in phenomena, explained briefly above. The classical definition has been that the vortex shedding frequency, f_s, of the vortices and the (actual) oscillation frequency, f, of the cylinder remain close to the natural frequency of the cylinder, f_N, and thus the ratio $f^\star = f/f_N \approx 1$. Whilst this interpretation has been true for high mass ratios, it is not for low mass ratios, as still significant amplitude response is evident despite the departure of the frequency ratio, $f^\star = f/f_N$, from unity. This behaviour of the frequency ratio can clearly be seen in Figure 2.5. For this reason, Govardhan and Williamson [37] choose to define synchronization as the matching of the frequency of the periodic wake vortex mode with the body oscillation frequency.

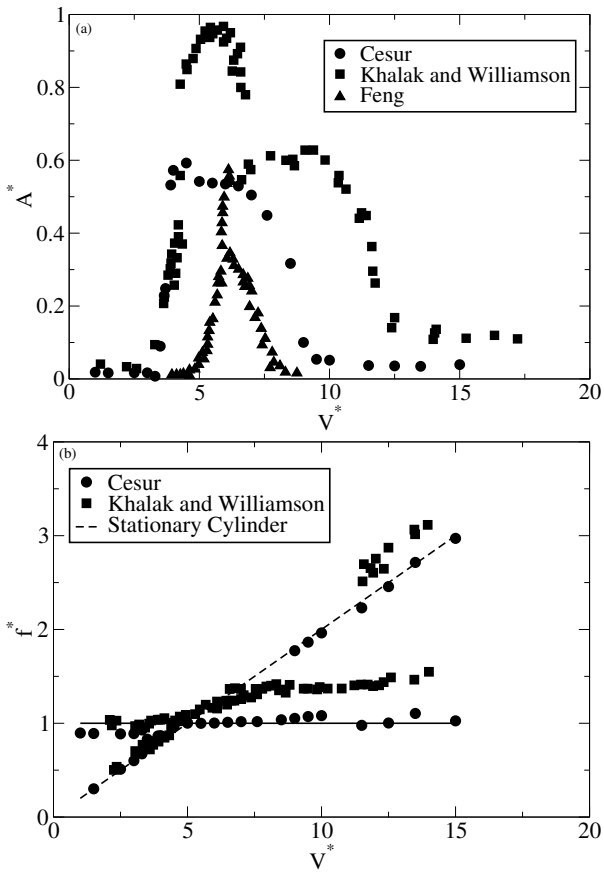

Figure 2.5: Response amplitude (a) and frequency (b) for an elastically mounted rigid cylinder. Symbols; ■: $m^\star = 2.4$ and $\zeta = 0.0045$ Khalak and Williamson [3] experimental data, ▲: $m^\star = 248$ Feng [4] experimental data, •: $m^\star = 2.7$ Cesur [5] numerical simulations. From Khalak and Williamson [3] with the addition of data from Cesur [5].

Elastically mounted cylinders vibrating at low mass ratios depict additional intriguing response behaviour. Earlier, it was mentioned that the vibrational response of an elastically mounted body may be determined using the reduced velocity, $V^\star$, which is related to the in vacuo natural frequency, f_N^v. Vikestad et al. [41] report in their experimental study

that at low mass ratios the in vacuo natural frequency is less relevant to use. Instead, the reduced velocity is often based on the natural frequency in still fluid, f_N^w, i.e. also accounting for the hydrodynamic mass as obtained using potential theory. For a cylinder the hydrodynamic mass is equal to the mass of the displaced fluid. Hence, since the cylinder also has to accelerate a portion of the surrounding fluid it appears to have a higher mass. The ratio between the two natural frequencies can therefore be written as

$$\frac{f_N^v}{f_N^w} = \sqrt{\frac{m + m_a}{m}} = \sqrt{\frac{m^\star + \pi/2}{m^\star}}. \tag{2.6}$$

However, it was shown by Vikestad et al. [41] that the hydrodynamic mass of a vibrating cylinder is not a constant, but instead depends strongly on the character of the vibrational motion. Vikestad et al. [41] show explicitly in their study how the equation of motion for a circular cylinder is reformulated to take into account for hydrodynamic mass and also damping as the reduced velocity is varied.

Response Dynamics: Dual Cylinders and 2DOF-Motions

It is expected that the complexity of VIV should increase considerably when two or more cylinders, elastically mounted, are arranged sufficiently close to each other, such that their wakes may interfere, and they can as a consequence vibrate as a coupled system.

Different interference effects between two cylinders can take place depending on whether if the cylinders are placed in a tandem, staggered or side by side configuration. Traditionally, focus has been made on tandem and staggered configurations. Borazjani and Sotiropoulos [42] have numerically investigated the VIV of two identical elastically mounted cylinders in tandem arrangement in both one (transverse) and two (transverse and streamwise) degree of freedom. The cylinders were placed $L/D = 1.5$ apart and the Reynolds number was $Re = 200$. They showed that the spacing ratio, L/D, plays an important role in the response amplitude. For the one degree of freedom (1DOF) system, it was shown that after some critical reduced flow velocity, $V^\star \geq 5$, the vortex shedding mechanism (which is the primary mechanism for the vibrations) was able to produce a vertical separation between the cylinders large enough to trig-

ger a secondary mechanism, i.e. the gap-flow mechanism. They observed that the criteria for the existence of the gap-flow and in turn high amplitudes was the appearance of a vertical separation of minimum one (cylinder) diameter between the oscillating cylinders. Both peak amplitudes and width of the synchronization range was enhanced when the cylinder configuration was altered from an isolated single to a tandem configuration. In particular, the addition of one more cylinder in the fluid domain was the cause of increased amplitude of oscillations of the rear cylinder.

The problem of an elastically mounted (single) cylinder vibrating transverse to a fluid flow has been the traditional way of examining VIV. A more practical problem is the body motion in two degrees of freedom (2DOF) such as riser tubes or heat exchangers, where the oscillating mass and the natural frequency is the same in the transverse and in-line directions. In contrast to these, the experimental works performed in the past with 2DOF-vibrations were based in principal on different values for the mass ratios and the natural frequencies in the transverse and in-line directions. The conclusions from the work of Sarpkaya [43], for example, was that bodies in 2DOF-motion do not lead to astonishing changes in the resonant amplitudes as compared to bodies in transverse-motion only. Among a few, one arrangement that ensures equal mass and natural frequency in both degrees of freedom is the pendulum set-up at Cornell university [44, 45, 46]. In these experiments, the Reynolds numbers ranged from 1000 to 15000, and the natural frequency and the oscillating mass in the two directions were typically $f_N = 0.4$ Hz and $m^\star$ ranged from 2.0 - 25.0, respectively. The study at Cornell university demonstrates that even at a range of low mass ratios ($m^\star \geq 6$), the freedom to oscillate in-line (streamwise) with the flow affects the transverse vibration very little. The same response branches, peak amplitudes, induced forces and vortex wake modes were found for both transverse-only and 2DOF-motion. However, a remarkable change was discovered in the fluid-structure interaction when the mass ratios were reduced below $m^\star = 6$. A new response branch with significant streamwise motion appears, in what they name the 'super upper' branch, yielding extremely large transversal amplitudes, $A^\star_{2DOF} \approx 1.5$, which is in excess of their typical transverse-only vibration ($A^\star_{1DOF} \sim 1$).

Wake Vortex Dynamics: Modes of Vortex Formation

There has been some debate in the literature regarding the structure of the vortices, i.e. the vortex formation modes, in the wake of vibrating cylinders that might be associated with different response branches. Williamson and Roshko [47] showed from their flow visualizations at high-$(m^\star\zeta)$ that the initial branch of the amplitude response is associated with a $2S$ mode indicating 2 single vortices shed per cycle, while the lower branch represents a $2P$ mode, i.e. 2 pairs of vortices are being shed per cycle. Also, Govardhan and Williamson [48] confirmed for low-$(m^\star\zeta)$, that the wake structures in the initial and lower branches correspond to the $2S$ and $2P$ vortex wake modes, respectively. In the upper branch, on the other hand, the structure corresponds to the $2P$ mode, where the second vortex of each pair is much weaker than the first one.

It is worth mentioning that many of the phenomena discovered for the elastically mounted cylinder carries across to more complex structures, including structures whose vibration amplitude varies along the span. Flemming and Williamson [6] studied the case of a pivoted cylinder free to move both streamwise and transversal to the flow. For cases with low inertia, $I^\star$, they observed the $2S - 2P$ hybrid mode similar to what was found for vibrating tapered cylinders by Techet et al. [49]. For the lightest structures, however, a new vortex formation mode was found along the span, the $2C$ mode. This mode comprises two co-rotating vortices each half cycle and corresponds to much larger transversal amplitudes, as well as enhanced streamwise vibrations. Moreover, the 'super upper' branch discovered by Jauvtis and Williamson [44, 45], as discussed earlier, is associated with a $2T$ vortex mode comprising two triplet of vortices in each half cycle, which also was found in the 2DOF-motion of the cylinders having uniform amplitude. These sets of vortex wake modes, $2S, 2P, 2C, 2T$, which are known to cause free vibration, at moderate Reynolds number, are shown in Figure 2.6.

In the section of Forced Cylinder Oscillations 2.2.2 the mode transitions (as a function of the reduced velocity) for low-$(m^\star\zeta)$, in contrast to one for high-$(m^\star\zeta)$ will be discussed in more detail.

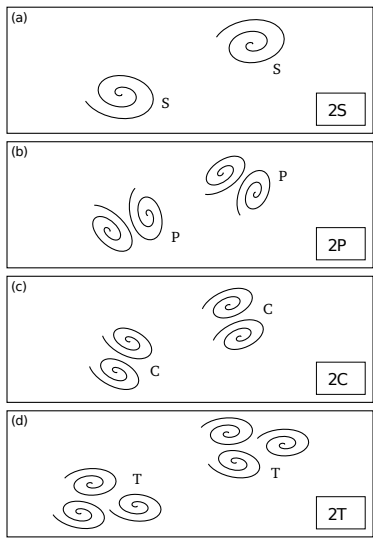

Figure 2.6: The set of vortex wake modes for a cylindrical structure. The $2C$ mode is found for the vibration of a pivoted cylinder (Flemming and Williamson [6]).

Reynolds number effect

So far, the characteristics of the amplitude and frequency response dynamics of an elastically mounted cylinder has been discussed and correlations for its associated wake vortex modes have been revealed. Many of the experiments and simulations conducted by the mentioned authors have drawn their conclusions based on high Reynolds number flows, typically in the range of $Re = 10^3 - 10^5$. The corresponding vortex-induced vibrations attained large transversal amplitude of oscillations, where values up to $A^\star \approx 1.5$ have been detected. Khalak and Williamson [33] have presented a table where they summarize peak amplitudes from various experiments and simulations. From this table it can be observed that Direct Numerical Simulations (DNS) of vortex-induced vibrations all yield a maximum peak amplitude around $A^\star = 0.6 - 0.7$ for $Re = 100 - 200$, which is significantly lower than the peak amplitudes found in experiments. Moreover, Williamson and Govardhan [37] compare the (so far

only) low-Reynolds number experiments by Anagnostopoulos and Bearman [50], over a range $Re = 90 - 150$, with 2D simulations in the range $Re = 100 - 200$ from other authors [51, 52, 53]. The conclusions are that no upper branch is seen when the peak amplitude, $A^\star$, is plotted against $(V^\star/f^\star)St$, whereby the amplitude response is solely determined by the initial and lower branches. Correspondingly, the $2P$ mode does not appear and instead the $2S$ and $P + S$ vortex formation modes constitute the wake structures.

2.2.2 Forced Cylinder Oscillations

The case of an elastically-mounted, rigid and freely-oscillating cylinder has served as a paradigm in the understanding of vortex-induced vibration problems in general. The vortex-induced motion and the wake of the (freely) oscillating body are intrinsically interdependent. This leads to a complicated relationship between these two factors which in turn becomes quite hard to determine. An approach to further understanding the fluid-structure interaction (between the oscillating rigid body and the wake) is to control the motion of the body, allowing the investigation to focus on the response of the wake to a pre-defined motion. A significant question arises when utilizing controlled oscillations, namely; if the forced motion captures the 'essential features' of the flow-induced motion, i.e. can the results of the forced oscillations be used to predict the motion of an elastically mounted rigid cylinder? This sought relationship between the forced and freely vibrating cases, especially the likelihood of the forced oscillation results to provide insight into the more complicated freely vibrating case, has been an important research area during the last decade.

It was shown in the work by Khalak and Williamson [33] for free vibrations (Figure 2.5) that strong flow-induced vibration occurs over a range of normalized free-stream velocities, $V^\star$ (and $\omega_N = 2\pi f_N$), typically in the lock-in region, where $f^\star = f/f_N \sim 1$. As $V^\star$ is varied the response of the cylinder, in particular the amplitude of oscillation, $A^\star = A/D$, varies significantly. The forced oscillations involve a different, but analogous, set of parameters. The forced cylinder oscillations are typically at a constant $A^\star$ while the frequency of forced oscillation,

f_e, is varied about the point where $f_e/f_s \sim 1$. Using the relationships stated above for the normalized flow parameters one can find a relationship between the independent variables for forced and free vibrations by assuming that the frequency of the forced oscillations, f_e, is equivalent to the oscillation frequency of the free motion, f. As a matter of fact, this can be shown via the relationship between $V^\star$ and $f^\star = f/f_N$ multiplied with the Strouhal number, St, yielding $(V^\star/f^\star)St = f_s/f$. Thus, $V^\star$ will vary inversely with f_e/f_s.

The transverse motion of a cylinder undergoing vortex-induced vibrations is generally sinusoidal and when the cylinder is forced to oscillate, this motion is approximated by a pure sinusoid. Hence, the approximated transverse force and the motion is often represented by

$$y(t) = A\, sin(2\pi f_e t), \tag{2.7}$$

$$F(t) = F\, sin(\omega t + \theta), \tag{2.8}$$

where A is the amplitude of oscillation, f_e is the frequency of oscillation, F is the instantaneous force and θ is the phase angle between the fluid force and the body displacement.

Carberry and Sheridan [54] have performed experiments on a circular cylinder forced to oscillate transverse to the free-stream at $Re = 2300$. The amplitude was held constant at $A^\star = 0.5$, while the frequency was varied over the range $0.5 \leq f_e/f_s \leq 1.4$. They discovered that the flow properties and the interaction between the natural instability of the wake and the forced oscillations depend strongly on the relation f_e/f_s. As the frequency ratio f_e/f_s was increased they were able to show an abrupt increase in C_L, which was approximately out-of-phase with the cylinder displacement, to a large amplitude in-phase lift force coefficient. Simultaneously, there was a sharp jump in the phase angle which shifted approximately 180°. Consequently, the sharp change in C_L was referred to as a transition from a low-frequency state to a high-frequency state of the lift force and the transitional frequency was measured to be in between $0.806 \leq f_e/f_s \leq 0.869$. Moreover, Carberry and Sheridan [54] also found a change of the vortex shedding pattern from $2P$ to $2S$ in the vorticity field when going from the low-frequency ($f_e/f_s \approx 0.806$) to high-frequency ($f_e/f_s \approx 0.869$) state. They associated this change to be related to the shift in the lift phase.

The use of time-averaged properties of the total lift force (2.8) and the structure of the near wake has been the traditional way of characterizing the wake states. An other way of describing the wake states is by using a combination of instantaneous values of θ_{lift} and θ_{vortex} and the corresponding wake structures. Essentially, the total lift force is made up of two components which can be treated separately: the vortex force which is due to changes in the position and strength of vortex structures in the wake, and the apparent mass force generated by the acceleration of fluid as the body accelerates, as discussed by Leonard and Roshko [55]. This yields the total force in terms of the lift force coefficients as

$$C_L(t) = C_{L_{vortex}}(t) + C_{L_{am}}(t), \tag{2.9}$$

When the wake is 'locked-on' to the motion of the cylinder, the total and vortex lift forces can be approximated by sinusoidal functions, introduced by Williamson and Govardhan [48] as follows:

$$C_L(t) \approx C_L \, sin(2\pi f_e t + \theta_L) \tag{2.10}$$

$$C_{L_{vortex}}(t) \approx C_{L_{vortex}} \, sin(2\pi f_e t + \theta_{L_{vortex}}). \tag{2.11}$$

Thus, $C_L(t)$ and $C_{L_{vortex}}(t)$ are the amplitude of the total and vortex lift force coefficients respectively, and θ_L and $\theta_{L_{vortex}}$ are the phase with respect to the displacement of the cylinder.

Carberry et al. [56] performed controlled oscillation of a cylinder transverse to the free-stream under the same experimental conditions as Carberry and Sheridan [54]. They were able to reveal a new wake state by instantaneous measurements of the total and vortex lift phases. The new state, named 'intermediate state', was found for $A^\star = 0.5$ (and also for $A^\star = 0.6$) and $f_e/f_s = 0.84$. It was shown that the development of the vorticity patterns for the intermediate state wake are different from those of both the low- and high-frequency wakes. However, the mode of the vortex shedding for the intermediate state was described as $2S$, where its' properties were found to be remarkably similar to the properties of the upper response branch of an elastically mounted cylinder described by Govardhan and Williamson [48].

In essence, Carberry et al. [57] have compared the wake states and response branches for forced and freely oscillating cylinders. Their objectives was to investigate whether the results of the forced oscillations

can be used to to predict the motion of an elastically mounted body. The results were presented from two different sets of experiments , where it should be mentioned that the two sets of experiments were not specifically designed for the purpose of their objectives. For forced oscillations, the frequency was varied between $0.74 \leq f_e/f_s \leq 1.27$ while the experiments were conducted at a number of oscillation amplitudes: $A^\star = 0.25$, 0.4, 0.5 and 0.6. The Reynolds numbers were varied between $Re = 2300$ to $Re = 9100$ for forced oscillations while for the elastically-mounted case Re varied between 3000 and 3700. The consideration of the total lift force as having two components, namely; the vortex force and the apparent mass force, allowed Carberry et al. [57] to reveal the intermediate state (as Carberry et al. [56]) and compare the variation of the total and vortex lift phases for the forced and freely oscillating cylinders. The (schematically) behaviour of the total and vortex phases in conjunction with the behaviour of the amplitude response for freely vibrating cylinder is shown in Figure 2.7(a-c) and can be summarized as follows:

- Low-Frequency State ⇔ Lower Branch: The mean vorticity fields for the low-frequency state and the lower branch correspond to shedding modes that at these oscillation amplitudes are $2P$.
- Intermediate State ⇔ Upper Branch: The mean vorticity fields for the intermediate and upper branch are $2S$ and $2P$, respectively.
- High-Frequency State ⇔ Initial Branch: The mode of vortex shedding for the high-frequency and initial branch wakes is $2S$.

In both forced and freely oscillating cylinders the jump in $\theta_{L_{vortex}}$ corresponds to the jump in the phase of vortex shedding. This is physically significant, as the vortex force is representative of the force due to the movement of vortex structures in the wake. This can be confirmed from Figure 2.7 (c) for freely vibrating cylinders, where the initial branch to upper branch transition is associated with a jump in $\theta_{L_{vortex}}$ and a change of vortex shedding mode takes place. The upper branch to lower branch transition, on the other hand, involves a jump in $\theta_{L_{total}}$ and no change of vortex shedding mode occurs. The behaviour for forced cylinder oscillation differs slightly. The high-frequency to intermediate state transition

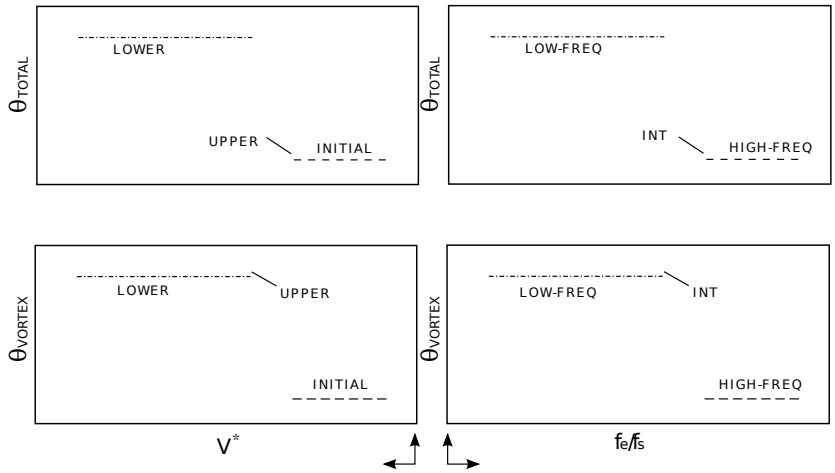

(a) Total and vortex phase for the freely vibrating cylinder.

(b) Total and vortex phase for the forced vibrating cylinder.

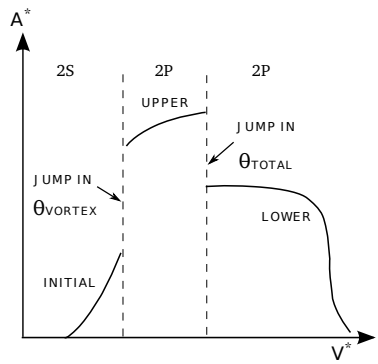

(c) Amplitude response for freely vibrating cylinder.

Figure 2.7: Schematic diagrams illustrating the behaviour of the total and vortex phases for (a) the free response branches at low-$m^\star\zeta$ values and (b) the corresponding forced wake states at a high $A^\star$, whereas (c) shows the amplitude response of the low-$(m^\star\zeta)$ type showing the principal branches, and correspondingly the jump phenomena.

is comprised of a jump in $\theta_{L_{vortex}}$, but no change of vortex shedding mode occurs, the wake is of a $2S$ character in both cases, in contrast to the freely vibrating cylinder. An analogous result is achieved for the intermediate to low-frequency state transition as can be seen in Figure 2.7 (a-b).

The extensive measurements of the fluid forces on a cylinder that is controlled to oscillate transverse to a free-stream by Morse and Williamson [58, 59] has recasted some additional findings for the fluid-structure interaction phenomena discussed above. They performed measurements of fluid forces on a cylinder that is controlled to oscillate transverse to a free-stream at $Re = 4000$. These measurements were used to create very high resolution contour plots of the magnitude of fluid forcing, and its phase relative to the cylinder displacement. In their investigation the amplitude ($A^\star$) is varied from 0.02 to 1.6. They were able to find clear discontinuities in the force contours, and hence were able to identify boundaries separating different fluid forcing regimes. These regimes appeared remarkably similar to boundaries separating different vortex shedding modes in the regime map of Williamson and Roshko [47]. One of the most striking findings of their study was an overlap region of the vortex shedding mode, lying between the $2P$ and $2S$ modes. They named this mode as '$2P_0$' mode which was a variation of the $2P$ mode, although there were two pairs of vortices shed per cycle, the secondary vortex was much weaker and decayed rapidly as the vortex pair moved downstream in the vortex wake. Further, the character of the $2P_0$ mode was stated to be equivalent to the 'intermediate wake state' identified by Carberry et al. [56] and the '$2P_{upper}$' mode found by Williamson and Govardhan [48]. Among else, Morse and Williamson [58, 59] visualize from their vorticity field that it is quite easy to mistake the $2P_0$ mode for a $2S$ mode depending on how well one has resolved the small secondary vortex.

Finally, at the introduction of this section an important question was underlined, namely; to what extent can measurements from controlled vibration be applied to the case of a freely vibrating, elastically mounted cylinder? The classical understanding of the question postulated has been, under the assumption that such motion is approximately sinusoidal, that the fluid excitation must be positive ($0° < [\theta_L$ and $\theta_{L_{vortex}}]$ $< 180°$), which is arisen from the property that the excitation energy,

C_E, is a function of the phase angle, i.e. $C_E \propto sin(\theta)$. Nevertheless, Morse and Williamson [58, 59] answered this question by examining the energy transfer from the fluid to the body motion. This was done by introducing the concept of an 'energy portrait', which is a plot of the energy transfer into the body motion and the energy dissipated by damping, as a function of normalized amplitude. They were able to define the complete regime in amplitude-wavelength plane in which free vibration may exist which requires not only positive excitation but also stability of the equilibrium solutions. It is, however, interesting to pay attention to the results of Carberry et al. [57], which compose forces and wake modes found for controlled vibration and free vibration oscillations. Carberry et al. [57] were able to find similar wake modes and jumps in the force and its phase, however, they also measured regimes of negative excitation from controlled vibration, suggesting that free vibration should not occur under the conditions at which free vibration has readily found. Most importantly, they concluded that sinusoidal controlled motion does not simulate all the key components of the flow-induced motion. This seems reasonable since the results were available at the time from different facilities. However, Morse and Williamson [60] made direct comparison between free and forced vibrations and were able to show that if the experimental conditions are matched exactly, controlled vibration can yield fluid forces which are in very close agreement with the results from free vibration. The key point in these kind of studies is a careful matching of conditions in order to be able to predict free vibration response with forced cylinder oscillations.

2.3 FSI on Flexible Cantilever

The flexible cantilever has received only little attention in the literature up till now. This configuration is, though, one of the most important examples of the general Vortex-Induced Vibrations (VIV) problems in fluid mechanics and yet it is still not been fully understood. One of the main questions to be answered is (as was mentioned in the beginning of this chapter) to be able to understand to what extent the rigid cylinder VIV behaviour is a valid hypothesis for predicting e.g. the response of a flexible cantilever structure with varying amplitude of deflection along

the span?

Studies concerning flexible cantilever cylinders have been tackled by for instance Pesce and Fujarra [7]. In their experimental study a clamped, lightly damped and long, flexible, circular cylinder was exposed to vortex-induced vibrations at Reynolds numbers varying from 6×10^3 to 4×10^4. They were able to detect 2 resonance branches, in accordance with experiments performed with rigid cylinders elastically mounted in linearly supports. In addition, they also observed a jump phenomenon within the synchronization region ($8.3 \leq V^\star \leq 10$) indicating that the lower and upper branches share the response amplitudes within this region. Moreover, from the experiments the maximum (transversal) modal amplitude occurred for $A^\star_{modal} \approx 1.27$.

A one-to-one comparison between the response amplitude for a flexible cantilever and an elastically mounted rigid cylinder was conducted by Fujarra et al. [10]. The cantilever data originated from the experimental study of Pesce and Fujarra [61], where same flexibility in the streamwise and transverse directions were employed whereas the rigid cylinder data was from Khalak and Williamson [8]. These experimental results are shown in Figure 2.8 where also the low Reynolds number ($Re = 400$) simulation by Revstedt [9] has been added. The response amplitudes reveal in average qualitatively similar behaviour for the flexible and rigid cylinders while it is hard to characterize the corresponding response for the cantilever beam with small aspect (i.e. length to diameter) ratio, ($AR_2 = 10$), due to lack of data.

Considering the response amplitudes of the two cylinders more careful, although the main difference seems to be in the larger maximum amplitude of oscillations for the cantilever, it is observed that the response of the cantilever exhibits only two branches, i.e. the initial and the lower branches, compared to the typical three-branch of response at low mass ratios for rigid cylinders. As a matter of fact, this happens to be true despite the fact that the cantilever is constructed in such a way that the mass ($m^\star$) and damping (ζ) of the cantilever are similar to the rigid cylinder's mass-damping parameter ($m^\star\zeta = 0.016$).

Besides comparing a flexible cantilever with same flexibility in the streamwise and transverse directions with an elastically mounted rigid

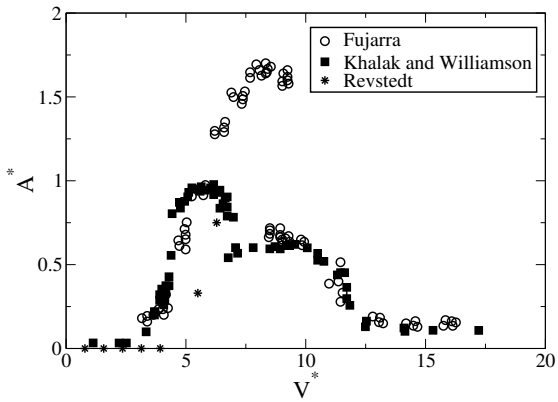

Figure 2.8: A comparison between amplitude response, $A^\star$, for a flexible cantilever and an elastically mounted rigid cylinder, as a function of normalized velocity, $V^\star$. Symbols; ○: Pesce and Fujara [7] data, ■: Khalak and Williamson [8] data, ⋆: Revstedt [9] data. From Fujarra et al. [10] and Revstedt [9].

cylinder Fujarra et al. [10] also studied the dynamic response of a flexible cantilever with enhanced stiffness and natural frequency in the streamwise direction and thereby restricting the vibrations of the body to principally transverse motion. It was found that the transverse amplitude response is similar to the vibrations of an elastically mounted rigid cylinder. Indeed, as the reduced velocity is increased a clear initial branch is reached extending to high reduced velocities with maximum amplitude of around $1D$ at $V^\star \approx 6$ and thereafter a jump to lower branch occurs. Furthermore, an interesting large-amplitude response mode was found outside the principal synchronization region at reduced velocities $V^\star \approx 12$. This effect, otherwise not seen for rigid cylinder was attributed to the stimulation of the streamwise oscillations which now is able to interact with the transverse oscillations. Indeed, the higher natural frequency in the streamwise direction shifts the regime of coupling to higher reduced velocities and the authors believe that this vibration mode may be related to a further vibration mode at high reduced velocities.

Considering the wake vortex dynamics for a flexible cantilever Yamamoto et al. [62] report recurrent findings of the formation of wake

modes. From their wake visualizations a hybrid mode of vortex shedding was found along the span of the cantilever. Following the terminology of Williamson and Roshko [47] a $2S$ mode was observed in regions of low amplitudes, typically at sections in the vicinity of the fix-end and extending towards the tip of the cantilever. For a given moderate reduced velocity (within the synchronization region) the $2S$ mode is transitioned into a $2P$ mode of vortex formation characterizing large-amplitude of oscillations. A further increase in the reduced velocity triggers the transition process to occur at an earlier stage, i.e. closer to the fix-end, leading to greater part of the cantilever being exposed to large amplitudes of vibrations.

CHAPTER 3

Fluid Motion

In the previous chapter a comprehensive description of the Fluid-Structure Interaction phenomenon was outlined from various experimental studies. In addition, some results were delivered from sporadic but relevant simulations. In these simulations a *mathematical model* is used to describe the motion of the fluids and the object from a physical point of view. In this chapter, the modelling and the set of equations governing the physics of fluid flows are described.

3.1 Governing Equations for Fluid Dynamics

Historically, there have been two different approaches taken to derive the equations of fluid dynamics: the phenomenological approach and the kinetic theory approach. In the phenomenological approach relations between the stress and rate of strain is postulated and the fluid dynamics equations are developed from the universal laws of conservation such as conservation of mass, momentum and energy, which has been thoroughly treated by Schlichting [63]. Hirschfelder et al. [64] describes, on the other hand, in detail the kinetic theory approach, in which the fluid dynamic equations are obtained with the transport coefficients defined in

terms of certain integral relations, which involve the dynamics of colliding particles.

In this thesis, the investigation of fluid dynamics is based on the phenomenological approach in correlation with the concept of *Reynolds transport theorem.* This concept requires a conversion of the mathematical formulations to be valid from a system analysis to a control volume analysis.

3.1.1 Fixed Mesh

Applying the Reynolds transport theorem to the balance laws of mechanics valid for a system and using the Gauss theorem assuming an infinitesimal control volume yields the conservation equations for a fluid flow. Presented on a form of Newtonian and incompressible fluid the conservation equations of mass (3.1) and momentum (also called Navier-Stokes) equations (3.2) take the following expressions in the Eulerian framework:

$$\nabla \cdot \mathbf{v} = 0, \tag{3.1}$$

$$\rho^f \frac{D\mathbf{v}}{Dt} = \nabla \cdot \boldsymbol{\sigma} + \mathbf{b}^f, \tag{3.2}$$

where, ρ^f, is the constant fluid density. Here, the divergence of the Cauchy stress tensor, $\boldsymbol{\sigma}$, and the external, velocity independent body forces, $\mathbf{b}^f$, balance the material derivative consisting of the partial time derivative of the fluid velocity, $\mathbf{v}$, and the convection term according to

$$\frac{D\mathbf{v}}{Dt} = \frac{\partial \mathbf{v}}{\partial t} + (\mathbf{v} \cdot \nabla)\mathbf{v}. \tag{3.3}$$

Application of the constitutive relationship provides the necessary closure of the governing equations. This is done by splitting the Cauchy stress tensor, $\boldsymbol{\sigma}$, into pressure, p, and a deviatoric viscous stress tensor, $\boldsymbol{\tau}^f$,

$$\boldsymbol{\sigma} = -p\mathbf{I} + \boldsymbol{\tau}^f. \tag{3.4}$$

For Newtonian fluids the viscous stress, $\boldsymbol{\tau}^f$, is a product of the dynamic viscosity, μ, and the strain-rate tensor, $\boldsymbol{\varepsilon}$, according to

$$\boldsymbol{\tau}^f = 2\mu\boldsymbol{\varepsilon} = \mu\left(\nabla\mathbf{v}^f + (\nabla\mathbf{v}^f)^T\right), \tag{3.5}$$

which in the end gives a linear relationship between the Cauchy stress tensor, $\boldsymbol{\sigma}$, and strain-rate tensor, $\boldsymbol{\varepsilon}$. It should be noted that the external forces, $\mathbf{b}^f$, are assumed to be insignificant and thus are neglected.

The conservation equations for mass and momentum presented in (3.1) and (3.2), respectively, have been formulated for the simulations of elastically mounted circular cylinders where the surface of the rigid body is represented using Immersed Boundary (IB) method and thus the simulations are conducted on a Cartesian fixed grid. However, for bodies deforming, as in the case of flexible cantilever beam, the fluid forces acting on the structure leads to the deformation of the structure. For this reason, the computational domain is no longer fixed but changes in time, which has to be taken into account. The approach for this obstacle is described in the following subsection 3.1.2.

3.1.2 Deforming Mesh

Arbitrary Lagrangian-Eulerian (ALE) is one of the most popular numerical techniques that is able to treat moving surfaces when objects are deformed. It is a concept that relies on moving-mesh utilities and is intended to cope with significantly distorted meshes when large deformations occur at the surface of an object.

The ALE equation of motion can be derived from the Eulerian formulation of the Navier-Stokes equations (3.2) by introducing a deforming reference system that follows the motion of respective boundaries. The re-formulated ALE formulation of the mass and momentum equations, for a time varying domain can be formulated as:

$$\nabla \cdot (\mathbf{v} - \mathbf{v}^m) = 0, \tag{3.6}$$

$$\rho^f \frac{\partial \mathbf{v}}{\partial t} + \rho^f [(\mathbf{v} - \mathbf{v}^m) \cdot \nabla]\mathbf{v} = \nabla \cdot \boldsymbol{\sigma} + \mathbf{b}^f, \tag{3.7}$$

where, $\mathbf{v}^m$, is the mesh velocity (at the deforming grid points) required to deform the fluid mesh. It should be noted that for an Eulerian formulation, $\mathbf{v}^m = 0$, and for a Lagrangian formulation, $\mathbf{v}^m = \mathbf{v}$. In the context of moving mesh, the mass conservation equation becomes independent of the mesh velocity, $\mathbf{v}^m$, and thus, doesn't introduce additional terms. The momentum equation, on the other hand, adds additional

constraint in the ALE approach. This leads to the system of governing equations (3.6) and (3.7) being not closed and hence the unknown mesh velocity, $\mathbf{v}^m$, has to be determined for. To compute this mesh velocity the so-called *geometric conservation law* (GCL) is used [65], which may be stated as "the change in volume (area) of each control volume between time t^n and t^{n+1} must equal the volume (area) swept by the cell boundary during $\triangle t = t^{n+1} - t^n$". In its differential form the GCL condition reads as

$$\frac{\partial V^e}{\partial t} + \nabla \cdot \mathbf{v}^m = 0, \tag{3.8}$$

where, V^e, is the volume of a control element which assures that within a change of a control element no space is lost.

Fluid Mesh Motion

Nominally, fluid-structure interaction problems are considered to be a two-field problem, which constitutes the solution of the flow and the solid equations. For deformable objects, though, the mesh motion is indeed considered as the third-field since its solution is non-trivial. The main objective of the mesh motion is to enable the structure to deform in response to the fluid stresses by maintaining the mesh quality close to the fluid-structure interface. Interface-tracking methods [66] are one approach that tracks the interface between the flow and the structure as the structure deforms. The mesh motion, in this thesis, is based on an Laplacian-approach developed by Jasak and Tukovic [67]. Shortly, the mesh elements are moved according to the diffusive Laplace equation as

$$\nabla \cdot (\chi \nabla \mathbf{v}^m), \tag{3.9}$$

where, χ, is the diffusion coefficient, equal to one, and is inversely proportional to the distance of the interface in square.

3.2 Numerical Methods and their Discretizations

The governing mass (3.1) and Navier-Stokes equations (3.2) form the mathematical model for the motion of fluids, as was discussed recently. They constitute a set of non-linear Partial Differential Equations (PDEs)

and can provide an analytical solution for the unknown parameters (velocity and pressure) only for very few simplified cases such as 2D potential flows. For time-dependent and flows with complex behaviour these PDEs are solved numerically in the context of Computational Fluid Dynamics (CFD). The unknown parameters are generally solved on a discrete set of points in space which comprise a *mesh*. Also, the time variable is discretized. Various discretization schemes may be used for this purpose, where the most common used schemes are Finite Differences (FD), Finite Elements (FE) and Finite Volumes (FV).

In this thesis, the simulations of the elastically mounted rigid circular cylinder, where an IB method represents the surface of the moving object, are conducted using the FD approach. An in-house code was used for this area. The simulations of the fluid dynamics for the flexible cantilever, on the other hand, are conducted using the FV approach at the price of lower accuracy when compared to finite differences. The OpenFOAM software package, which is based on C++ programming language, was chosen as the CFD tool box. Moreover, the solution of the unknown (displacements) for the flexible cantilever are calculated using the FE approach and is, as the fluid counterpart, based on C++ language as well. OOFEM is the name of the software package that is used to solve the deformations, which is a finite element code with object oriented architecture. Furthermore, it is as OpenFOAM, an Open Source code with libraries including mechanical, transport and fluid mechanics solvers.

A side-note; To distinguish the two types of simulations used in this thesis the solvers used for the fluid-structure interaction in the simulations of the elastically mounted rigid circular cylinder and flexible cantilever exposed to cross-flow will hereafter be denoted as FSI-solver1 and FSI-solver2, respectively.

3.2.1 Finite Differences and Staggered Grid Formulation

For the discretization of the fluid part of the FSI-solver1 a Finite Difference scheme has been used to the set of governing equations (3.1,3.2) which take the following non-dimensional forms:

$$\nabla \cdot (\mathbf{v}^{\star}) = 0, \tag{3.10}$$

$$\frac{\partial \mathbf{v}^\star}{\partial t^\star} + (\mathbf{v}^\star \cdot \nabla)\mathbf{v}^\star = -\nabla p^\star + \frac{1}{Re}\left(\nabla^2 \mathbf{v}^\star\right) + \mathbf{\Phi}, \tag{3.11}$$

where $\mathbf{\Phi}$ are momentum source terms, which will be explained further in Chapter 6. For the non-dimensionalization procedure, see PAPER4.

The finite difference approximation to the Navier-Stokes equations (3.11), defined in the Cartesian frame work, leads to a discrete set of algebraic equations, which at position i and time n can be written as

$$\mathcal{T}^p(\phi) + v_i^n \mathcal{C}^q(\phi) = -\mathcal{Q}^w(\phi) + \alpha \mathcal{D}^r(\phi), \tag{3.12}$$

where $\mathcal{T}$, $\mathcal{C}$, $\mathcal{Q}$ and $\mathcal{D}$ are difference operators for the temporal, convective, pressure and diffusive terms, respectively, and the superscripts p, q, w and r stand for the order of accuracy in relation to the mesh spacing.

For solving the governing equations of fluid mechanics numerically, the continuous derivatives of continuity- and the momentum equations are discretized on a fixed Cartesian staggered grid. It is a mesh with equally spaced grid points, i.e. $\triangle x = x_{i+1} - x_i = \triangle y = y_{i+1} - y_i = h$. Such a grid is characterized by a structured mesh and composed of hexahedral cells (in $3D$), where the dependent velocity components are computed on the cell faces and pressure is computed at the center of the control volume, as shown in Figure 3.1. The main advantage of using a staggered grid, apart from its high accuracy capability, is that odd-even decoupling between the pressure and the velocity, which leads to checkerboard oscillations, can be avoided. Nevertheless, a disadvantage with staggered grids is that it might be difficult to represent complex boundaries accurately.

Spatial discretization

The spatial discretization is performed by finite differences using local Taylor-series expansion of the derivatives in (3.10) and (3.11). Using a second order central difference scheme to discretize the convective terms in the momentum equations may under certain conditions lead to numerical instabilities. These instabilities can be avoided if the convective terms are instead discretized in such a way that they are discretized using

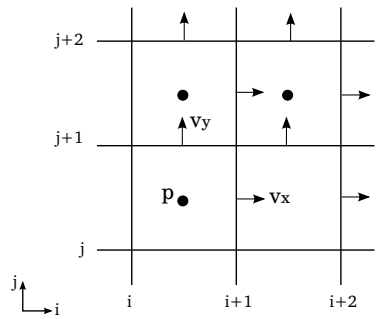

Figure 3.1: Two-dimensional staggered finite-difference grid.

a first order upwind scheme,

$$\left(v\frac{\partial\phi}{\partial x}\right)_i \approx v_i C^1(\phi) = v_i\,\frac{\phi_i - \phi_{i-1}}{h} + T.E., \tag{3.13}$$

$$T.E. = -\frac{1}{2}\,|v\,|h\frac{\partial^2 v}{\partial x^2} + O\left(h^2\right). \tag{3.14}$$

where the second derivative in the leading term of the truncation error (T.E.) implies numerical dissipation and hence numerical stability.

First order accuracy is not clearly adequate from an accuracy point of view and therefore higher order discretization is required. A third order upwind scheme proposed by Rai and Moin [68] is applied to the convective term

$$\begin{aligned}\left(v\frac{\partial\phi}{\partial x}\right)_i &\approx v_i C^3(\phi) = v_i\frac{\left(\phi_{i-2} - 8\left(\phi_{i-1} - \phi_{i+1}\right) - \phi_{i+2}\right)}{12h}\\ &+ |\,v_i\,|\,\frac{\left(\phi_{i+2} - 4\left(\phi_{i-2} + \phi_{i-1} + \phi_{i+1}\right) + 6\phi_i\right)}{12h} + O\left(h^3\right),\end{aligned} \tag{3.15}$$

where the leading term of the truncation error $(-\frac{1}{12}\,|v\,|h^3\frac{\partial^4 u}{\partial x^4})$ includes the fourth derivative, and is hence dissipative.

The diffusive and the pressure terms, $\mathcal{D}^4(\phi)$ and $\mathcal{Q}^4(\phi)$, are discretized using a standard fourth order central scheme.

Defect correction

A direct application of the higher order discretization schemes may lead to a less robust solver with considerably slower convergence rate. Instead, Fuchs [69] introduced a so-called "single-step" defect correction in order to combine numerical stability and efficiency of the lower-order schemes while maintaining higher order accuracy. The equations are solved using first and second order schemes, however, with a RHS according to (3.17)

$$\mathcal{T}^p(\phi)_i^n + v_i^n \mathcal{C}^1(\phi)_i^n - \alpha \mathcal{D}^2(\phi)_i^n = \mathcal{E}_\phi. \tag{3.16}$$

Here $\mathcal{E}_\phi$ is the defect correction term which is defined as the difference between the higher and the lower order discrete approximations of the previous time step

$$\mathcal{E}_{(\phi)} = v_i^{n-1} \left(\mathcal{C}^1(\phi)_i^{n-1} - \mathcal{C}^3(\phi)_i^{n-1} \right) - \alpha \left(\mathcal{D}^2(\phi)_i^{n-1} + \mathcal{D}^4(\phi)_i^{n-1} \right). \tag{3.17}$$

The iteration process is continued until $|(\phi)_i^n - (\phi)_i^{n-1}| < \delta$, (where δ is a prescribed small number) at which time the low order terms almost cancel. Also, note that the higher order terms can be set to any order of accuracy.

Temporal discretization

The computational code used in this thesis utilizes a three level second order implicit scheme for the discretization of the temporal derivative, $\mathcal{T}^2(\phi)$;

$$\left(\frac{\partial \phi}{\partial t} \right)^{n+1} \approx \frac{3\phi^{n+1} - 4\phi^n + \phi^{n-1}}{2\triangle t} + O\left(\triangle t^2\right). \tag{3.18}$$

Fluid Solver

For incompressible flows the solution of the system of governing equations require an explicit coupling between the pressure and velocity in the otherwise unbalanced equations. This is done by solving the classical Poisson equation, where the Laplacian ($\nabla^2 p$) of the pressure is explicitly expressed in terms of the velocity.

The solution procedure of the system of equations is based on the SIMPLE algorithm from Patankar [70], which is a segregated approach for the evaluation of the approximate relation between the necessary (predictions and) corrections for pressure and velocity. It is necessary in the sense that momentum- and the continuity balance need to be satisfied due to the segregated approach. In conjunction with the SIMPLE algorithm a multi-grid method is used that employs the Gauss-Seidel relaxation technique iteratively. The overall purpose of the multi-grid approach is to accelerate the solver, where the Gauss-Seidel scheme smooths the approximations in the sense that local high-frequency errors in the solution is reduced. Subsequently, the low-frequency errors are reduced at a rate inversely to the number of cells [71].

3.2.2 Finite Volumes and Collocated Grid Formulation

The computational domain of the fluid part in FSI-solver2 utilizes the Finite Volume method to formulate the solution domain, (3.6) and (3.7), in control volumes. Here, the solution is sought at points/nodes positioned in the centre of these volumes. An unstructured mesh consisting of tetrahedral elements have been used for this purpose, although general polyhedral shapes are available for the description of control volumes in OpenFOAM. Moreover, the grid is of collocated type, i.e. all dependent variables share the same control volumes [72]. Furthermore, the solution equations are re-formulated for a temporally varying domain, i.e. control volumes with time-dependent volumes V(t) and surfaces S(t).

The FV method discretizes an integral form of the governing equations leading to conserved properties of the quantities in the mass and momentum equations, (3.6) and (3.7), respectively. The corresponding discretized mass and momentum equations take the following form

$$\sum_f (\mathbf{v} \cdot d\mathbf{A})_f^{n+1} = 0, \tag{3.19}$$

$$\sum_{i=0}^{m}(\alpha_i(\mathbf{v})_p^{n+i} + \frac{\beta_i \triangle t}{V_p}\sum_f[(((\mathbf{v}_f - \mathbf{v}^m)\cdot d\mathbf{A}_f)\mathbf{v}_f) - \\ (\nu_{eff})_f(\nabla\mathbf{v})_f]^{n+i}) = \triangle t\sum_{i=0}^{m}(\beta_i(-(\nabla p)_p^{n+i})), \tag{3.20}$$

after Gauss theorem together with a multi-step time-integration method being used [73]. The reader is referred to PAPER1 for more detailed information.

Spatial Discretization

The Navier-Stokes equations in (3.7) are of second order as the diffusion term includes the second derivative of a generic variable, say $\phi = \mathbf{v}$. To achieve a satisfactory numerical accuracy the order of the discretization method needs to be equal to or higher than the order of the equation that is being discretized. In (3.20), a Gaussian integration scheme of 2nd order was used for the discretization of the convective term. However, the accuracy of the discretization method depends on the assumed variation of the function $\phi = \phi(\mathbf{x}, t)$ in space and time around a point P [72]. In order to obtain at least a second-order accurate method, a linear variation must be fulfilled in both space and time. This is understood if the Taylor series expansion in space of a function around a point $\mathbf{x}$ is considered:

$$\phi(x) = \phi_p + (\mathbf{x} - \mathbf{x}_p).(\nabla\phi)_p + T.E., \tag{3.21}$$

where $T.E. = \frac{1}{2}(\mathbf{x} - \mathbf{x}_p)^2 : (\nabla\nabla\phi)_p$ and the operator ": " is the inner product of two 2nd rank tensors, creating a scalar. Clearly, the truncation error (T.E.) shows that function $\phi(x)$ is 2nd order-accurate in space. It is assumed that the same holds in time.

The discrete set of the convective term in (3.20), require the variable ϕ to be evaluated in the center of a (2D) face which is shared between two (3D) volume cells based on a three-dimensional control volume. This interpolation procedure can be done, among else, *linearly* as was mentioned above. Indeed, OpenFOAM provides a variety of interpolation routines, e.g. upwinded convection schemes, TDV schemes and NDV schemes, where each of these contain further subcategories.

Figure 3.2 shows the linear, also called Central Differencing (CD), scheme applied between two cells with centres P and N that share the face f. The corresponding interpolation obeys as [72]

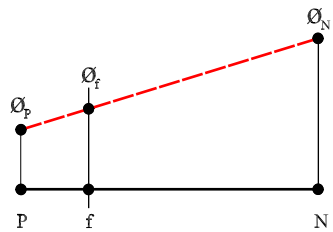

Figure 3.2: Face Interpolation scheme.

$$\phi_f = f_x \phi_p + (1 - f_x)\phi_N, \tag{3.22}$$

where $f_x = \overline{fN}/\overline{PN}$ and is defined as the ratio between the two distances, $\overline{fN}$ and $\overline{PN}$. It is known that second order accuracy schemes can cause non-physical oscillations. An alternative interpolation scheme that might be the Upwind Scheme (UD),

$$\phi_f = \begin{cases} \phi_p, & \text{if } F \geq 0\,, \\ \phi_N, & \text{if } F < 0\,, \end{cases} \tag{3.23}$$

where F represents the mass flux through the face. Although this scheme ensures for boundedness the face values of ϕ_f are obtained with only first order accuracy.

The Blended Differencing scheme (BD) offers a possibility to preserve both boundedness (UD scheme) and accuracy (CD scheme) of the solution via a blending factor, γ:

$$\phi_f = (1 - \gamma)\phi_{f_{UD}} + \gamma\phi_{f_{CD}}. \tag{3.24}$$

It can clearly be seen that depending on the value of γ, $0 \leq \gamma \leq 1$, a diffusive (UD) scheme, $\gamma = 0$ or a dispersive (CD) scheme, $\gamma = 1$, is obtained. In this thesis, γ equal to 0.3 has been used throughout the investigation in all papers.

The diffusive term, $(\nabla\phi)_f$, is decomposed into orthogonal and non-orthogonal parts to minimize the non-orthogonality error. Central difference approximations are applied to the orthogonal part while face interpolation of the gradients of the dependent variables is used for the non-orthogonal parts.

Temporal Discretization

The temporal terms are discretized using the implicit 2nd order (implicit Backward) scheme, which in a discretized form can be written as

$$\left(\frac{\partial\phi}{\partial t}\right)^{n+1} = \frac{3\phi^{n+1} - 4\phi^{n} + \phi^{n-1}}{2\triangle t}, \tag{3.25}$$

where the indices $n+1$, n and $n-1$ correspond to time levels $t+\triangle t$, t and $t-\triangle t$, respectively.

Fluid Solver

The solution procedure of the discretized set of governing equations are solved sequentially. Moreover, the required pressure-velocity coupling is done using the PISO algorithm in FSI-solver2 [74], whereas a PIMPLE algorithm [74], which is a merged PISO-SIMPLE method, has been used in the CFD simulations of a stiff cantilever beam.

CHAPTER 4

Turbulent Flows

4.1 Phenomenological Description

Flows occurring in industrial facilities, and also in nature, are mostly of turbulent character. In general terms, turbulence, which is a property of the flow and not the fluid, occurs beyond a certain threshold when the viscous forces are no longer able to damp out the flow instabilities caused by disturbances. Depending on the flow conditions, this threshold becomes case-specific and varies for e.g canonical pipe flows and flows past rigid objects with various shapes. It can be observed that beyond this critical threshold, which is determined by the Reynolds number (2.1), the flow regime exhibits a three-dimensional character with highly irregular and random motions making statistical methods a necessity in the analysis and quantification of such flows. Moreover, turbulent flows are dissipative/diffusive and unlike laminar flow regimes, the chaotic motions consist of a wide range of length- and time scales that need to be considered a priori.

Energy Cascade and Scales in Turbulence

Traditionally, the various length scales of turbulent structures have been categorized by means of the cascade of their energy contents. This is quite a central procedure in the analyses of turbulent flows and demonstrates how the kinetic energy of turbulent fluctuations is being transferred by a break-up process of the largest eddies, which are restricted by the flow geometry, to the smallest scales at which the kinetic energy is dissipated into heat by a viscous process. Nevertheless, it is not always the case that energy becomes transferred from eddies of large scales to the small scales. The reverse process, i.e. energy being transferred from the small scales to the larger ones, may also be encountered. This phenomenon, named as *backscatter*, is important and needs to be considered when dealing with numerical solutions of turbulence flows.

Although in general, the large eddies are anisotropic for sufficiently large Reynolds number, the small-scale turbulent motions can be approximated as statistically isotropic according to Kolmogorov's hypothesis of local isotropy [75]. This assumption leads to the definition of the energy spectra for various scales and the ranges as shown in Figure 4.1 and presented below.

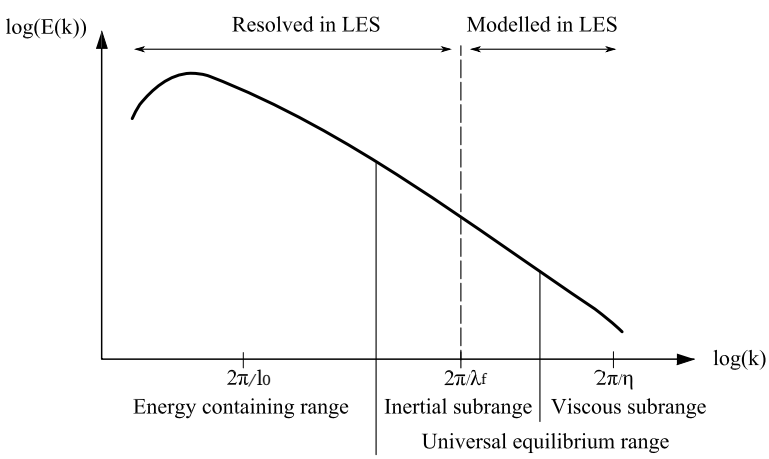

Figure 4.1: Energy spectrum of turbulent flow, $E(k)$, as a function wave number, k.

Energy containing range

The turbulent kinetic energy is mainly produced at the largest eddies, referred to as *integral length scale* and denoted as l_0 and belonging to the energy containing range in the energy spectrum (Figure 4.1). In homogeneous isotropic turbulence with zero mean velocity, the size of these scales can be estimated via a spatial autocorrelation function:

$$f(r) = \frac{\overline{v'(x)v'(x+r)}}{\overline{v'(x)v'(x)}}, \tag{4.1}$$

where v' is the velocity fluctuation at a given point, r is the distance from the point x and the overbar denotes a time average operation. The integral length scale is therefore the integral of the autocorrelation function as

$$l_0 = \int_0^\infty f(r)\, dr, \tag{4.2}$$

which represents the mean distance at which the velocity fluctuations are correlated in the flow.

Viscous subrange

The viscous subrange is dominated by the (smallest) Kolmogorov scales which are uniquely determined by the (kinematic) viscosity, ν, and the dissipation rate, ϵ, according to Kolmogorov's first similarity hypothesis. At these scales, the eddies do not break up further, instead, the turbulent kinetic energy is converted into heat by viscous dissipation. Appropriate dimensions for the Kolmogorov scales is obtained by combining ϵ and ν according to:

$$\eta \equiv \left(\frac{\nu^3}{\epsilon}\right)^{1/4}, \quad t_\eta \equiv \left(\frac{\nu}{\epsilon}\right)^{1/2}, \quad v_\eta \equiv \left(\frac{\eta}{t_\eta}\right) = (\nu\epsilon)^{1/4}, \tag{4.3}$$

where η, t_η and v_η are the length, time and velocity scales, respectively.

Inertial subrange

Kolomogorov's second similarity hypothesis states that at sufficiently high Re number there exist a range of scales such that $\eta \ll l \ll l_0$,

where the statistics of the fluid motion is uniquely determined by the dissipation rate of the turbulent kinetic energy, ϵ, independently of the viscosity, ν. The *Taylor length scale*, λ_f, belongs to this range, at which inviscid processes are dominant and external factors such as boundary conditions do not influence the scales. The characteristic length scale can be defined as:

$$\lambda_f^2 = \frac{-2}{d^2\, f(r)/dr^2|_{r=0}}, \tag{4.4}$$

which is based on the second derivative of the autocorrelation function at $r = 0$ in (4.1). The Taylor length scale has no clear physical interpretation [75], however, it can be a useful reference when estimating the required spatial resolution for large eddy simulation (LES).

The inertial and viscous subranges are categorized under a particular name according to Kolmogorov's hypotheses; the *universal equilibrium range*. By the name, this is the range where turbulence is in equilibrium in the sense that the production of turbulent kinetic energy equals the dissipation rate. The corresponding energy spectra associated with the inertia subrange is given by

$$E = \epsilon^{2/3}(k)^{-5/3}, \tag{4.5}$$

where k is the wave number and related to the length scales λ by $k = 2\pi/\lambda$ in Figure 4.1.

4.2 Large Eddy Simulation

It was shown that turbulent flows for sufficiently high Reynolds numbers involve a wide range of scales in time and space, extending from the largest integral length scales to the smallest ones, i.e. Kolmogorov scales. Except for very low Reynolds numbers, it is not feasible from a computational framework to resolve all the scales down to the Kolmogorov scales. Additionally, the smallest scales might not always pertain any significant role in the overall dynamics of the fluid flow. Instead, one might be interested in the behaviour of the larger scales that might interact with for example a vibrating or deformable body. Therefore, techniques are nowadays available which model the unresolved scales instead of resolving them.

Since turbulent flows only have meaning in a statistical sense, the average quantities of the dependent variables become of interest. Consider a generic variable that can be decomposed into its averaged, $\tilde{f}$, and fluctuating, f', components such that:

$$f = \tilde{f} + f'. \tag{4.6}$$

Different filtering procedures, in addition to time averaging, exist and when these are applied to the governing equations of fluid motion in (3.1) and (3.2) each of them lead to distinct different solution approaches in the CFD framework. The corresponding solution approaches can be summarized as follows:

- Temporal/Ensemble averaging $\Longleftrightarrow$ (RANS/URANS)
- Spatial filtering $\Longleftrightarrow$ (LES)
- No-averaging, completely resolved $\Longleftrightarrow$ (DNS)

The outcome from filtering and averaging procedures is, generally speaking, to introduce additional terms called turbulent stress tensors, i.e. $\boldsymbol{\tau}_T = \widetilde{\mathbf{v}\mathbf{v}} - \tilde{\mathbf{v}}\tilde{\mathbf{v}}$, where the unknown quantities, $\widetilde{\mathbf{v}\mathbf{v}}$, make the set of governing equations "unclosed". Hence, the essence of turbulence modelling becomes the one of expressing the unknown terms as a function of the filtered variables and their derivatives.

In Reynolds Averaged Navier-Stokes (RANS) equations, where the instantaneous governing equations are 'filtered' in time, the averaging procedure introduces an extra unknown quantity called the *Reynolds stresses*. The approach relies on the modelling of the unknown term by 'discarding' all of the scales at the averaging procedure in the turbulent spectrum, see Figure 4.1. The most used models within RANS framework are the Reynolds stress models, and two equation models. The main drawback with RANS is the lack in capturing the transient dynamics most often associated with the unsteady fluctuations.

In Direct Numerical Simulations (DNS), on the other hand, all of the scales down to the Kolmogorov scale are resolved. In physical space the resolution of the smallest dissipative motions requires a sufficiently grid spacing, i.e. $\triangle x \approx 2.1\eta$ [75]. Nevertheless, the profit in detailed resolution of the turbulent scales is inhibited in the computational effort as the

total contribution of spatial and temporal computations yield operations being proportional to $\sim Re^3$.

Explicit Filtering of LES and SGS models

The existence of the inertial subrange (Figure 4.1), where the small scales have a universal character, is appealing from the modelling point of view. Indeed, this property is exploited in the LES approach.

As discussed earlier, in LES the instantaneous governing equations are filtered by employing an (explicit) spatial filter (either spectral or in physical space):

$$\tilde{f}(x) = \int f(x')F_{\triangle}(x - x')dx', \tag{4.7}$$

where $F_{\triangle}$ is the LES filter kernel whose filter width, $\triangle$, can either be fixed or adaptive. The most commonly used explicit filters are the top-hat and the Gaussian filter in the physical space and the cut-off filter in the spectral space. As mentioned above, the filtering introduces unknown terms in the governing equations according to

$$\nabla \cdot \tilde{\mathbf{v}} = 0, \tag{4.8}$$

$$\frac{\partial \tilde{\mathbf{v}}}{\partial t} + (\tilde{\mathbf{v}} \cdot \nabla)\tilde{\mathbf{v}} = -\nabla \tilde{p} + \nabla \cdot (\nu \nabla \tilde{\mathbf{v}}) - \nabla \cdot \tilde{\boldsymbol{\tau}}_T + \tilde{\mathbf{b}}, \tag{4.9}$$

where $\tilde{\boldsymbol{\tau}}_T = \widetilde{\mathbf{v}\mathbf{v}} - \tilde{\mathbf{v}}\tilde{\mathbf{v}}$ is the unclosed term that represents the unresolved sub-grid-scales fluctuations and is normally called the sub-grid scale stress (SGS) terms that needs to be modelled. Several SGS-models have been presented in the literature and a good overview is presented by Pope [75]. Among these are the Smagorinsky model, Germano's Dynamic model and the Scale Similarity model. In a concise manner, what can be said about the role of the SGS-models in general are, except for representing the effect of the unresolved scales on the resolved ones, to supply the turbulent kinetic energy of the fluctuations with correct amount of dissipation, take into account for backscatter and also provide adaptivity for low Reynolds numbers flows.

It is not the intention to go through the details of these models, instead the reader is referred to the literature [75].

Implicit Filtering of LES

The idea with implicit filtering is that the discretized numerical schemes replace the role of the (explicit) SGS-models, which is to account for dissipation of turbulent kinetic energy at small scales and to account for the effects of the unresolved scales on the resolved ones. In this case no SGS-models are used and hence, the filtered field variables in (4.8) and (4.9) are equivalent with the discretized field variables

$$\tilde{f} \equiv \mathcal{D}(f), \tag{4.10}$$

where $\mathcal{D}(\cdot)$ is a discretization operator. It may be shown that as the grid size is decreased the effect of the SGS-terms is of the same order of the truncation error introduced by the discretized numerical schemes, e.g. the T.E. error in the convective term used in the in-house code and the blended scheme in OpenFOAM, discussed earlier. Thus, numerical schemes include the necessary dissipation representative for the smallest scales and thereby ensuring that no accumulation of turbulent kinetic energy will take place which otherwise will cause divergence of the numerical solution procedure.

For ILES schemes it is important that the amount of dissipation is not too large. This puts a restriction to have adequate grid resolution such that considerable part of the turbulent energy spectrum is resolved. This can be achieved by employing discretization schemes of high order accuracy enough such that its spectral behaviour damp only modes that are about or in the best way equal to the grid size, i.e. $\triangle \approx h$. Thus, if the spatial resolution is of the Taylor scale the rate at which energy is cascaded to the small scales becomes solely dependent of the physics only and hence, the effects of the numerical viscosity (the effect of SGS-terms) on the larger eddies can be neglected.

CHAPTER 5

Solid Body Motion

This chapter treats the governing equations, which model the motion of a solid body, and the corresponding numerical formulations. Firstly, the underlying theory of the mathematical model for the deformations of the flexible cantilever beam is presented. Thereafter, a numerical section provides the approximate discrete formulations of the mathematical equations.

5.1 Theory of Solids and their Deformation

The goal here is to determine the large-deformation (with a specific measure) of a continuous body in the finite element (FE) context, which is established by accounting for the geometric non-linearity in the formulation of the equilibrium equations.

Most commonly, the structural equations are described using Lagrangian frame-of reference, where material derivative in (3.3) becomes only a partial derivative with respect to time, such that the momentum equations become

$$\rho^s \ddot{\mathbf{u}} = \nabla \cdot \boldsymbol{\sigma} + \rho^s \, \mathbf{b}^s. \tag{5.1}$$

Here, ρ^s denotes the density of the structure, $\mathbf{u}$ the displacement of the material point in space, $\mathbf{b}^s$ the external body forces (which are assumed to be of insignificant size) and $\boldsymbol{\sigma}$ is the (symmetric and) second order Cauchy stress tensor defined in the current configuration.

However, it is desirable to seek a stress tensor in the reference configuration instead, while maintaining its' symmetrical properties. Making use of Cauchy's theorem and Nansons formula [76], the Cauchy's stress tensor $\boldsymbol{\sigma}$ is transformed into a second order tensor referred to as the *second Piola-Kirchhoff stress* tensor defined as, $\mathbf{S} = \mathbf{F}^{-1}\,\mathbf{P}$, where $\mathbf{F}$ and $\mathbf{P}$ are known as the deformation and *first Piola-Kirchhoff stress*, tensors, respectively. Inserting the second Piola-Kirchhoff stress tensor relation into (5.1) brings the symmetrical tensor properties to the equation of motion

$$\rho^s \ddot{\mathbf{u}} = \nabla \cdot (\mathbf{SF}) + \rho^s\,\mathbf{b}^s. \tag{5.2}$$

5.1.1 Total Lagrangian Formulation

In this thesis the Total Lagrangian (TL) formulation has been used to describe the motion of the material points. The TL method describes the motion by the total displacement field, $\mathbf{u}(\mathbf{x}_0)$, with respect to the initial (reference) position, $\mathbf{x}_0$, of the material point. Another formulation is the Updated Lagrangian (UL) formulation, where the material points are referred to the current position, i.e. the last-calculated configuration. The difference between the two methods lies in their numerical efficiency [77]. The TL method generally requires more memory but less computational time than the UL method because spatial derivatives are with respect to a fixed frame and thus need to be computed once. The UL method, on the other hand, requires updated derivatives each iteration because the reference configuration changes.

Furthermore, concerning the physical quantities such as stress and strain, the TL formulation leads naturally to deformations described in terms of the Green strain tensor, $\mathbf{E}$, corresponding to the conjugate Piola-Kirchhoff stress tensor, $\mathbf{S}$.

Multiplying (5.2) with a virtual displacement, $\delta\mathbf{u}$, and integrating over the initial volume using Green-Gauss theorem together with the

divergence theorem [78] results in the following virtual work expression

$$\int_v \rho\, \delta\mathbf{u}^T\, \ddot{\mathbf{u}}\, dv + \int_v \hat{\mathbf{E}}^T\, \mathbf{S}\, dv - \int_s \delta\mathbf{u}^T \mathbf{t}\, ds - \int_v \rho\, \delta\mathbf{u}^T \mathbf{b}\, dv = \mathbf{0}. \tag{5.3}$$

For this dynamic loading situation, any lack of equilibrium may be considered equivalent to a distribution of residual forces, $\mathbf{r}(\mathbf{x}_0)$, accounting for the difference in the internal, $\delta\mathbf{V}_{int} = \int_v \hat{\mathbf{E}}^T\mathbf{S}\, dv$, and external virtual work, $\delta\mathbf{V}_{ext} = \int_s \delta\mathbf{u}^T\mathbf{t}\, ds - \int_v \rho\, \delta\mathbf{u}^T\mathbf{b}\, dv$, plus a virtual loading, $\delta\mathbf{V}_{dyn} = \int_v \rho\, \delta\mathbf{u}^T\, \ddot{\mathbf{u}}\, dv$. For a solid body, with suitably discretized displacement field and loading, the Newton-Raphson method can be used to eliminate a discrete set of residual forces and hence establish equilibrium. This is, among else, covered in section 5.2.

5.1.2 Constitutive Relationship and Element Formulation

So far, nothing has been mentioned about the material model used in the structural analysis of the solid. Throughout in this thesis, an isotropic and linear elastic material model has been used to link the material stresses to its strain law and thereby closing the set of equations in (5.2). A suitable strain measure for the symmetric second Piola-Kirchhoff stress tensor is the Green-Lagrange's strain, which is invariant to body rotations. Evidently, a one-to-one (linearly) relation between the symmetric second Piola-Kirchhoff stress and the Green-Lagrange's strain can be established (in matrix form) as

$$\mathbf{S} = \mathbf{D}\mathbf{E}, \tag{5.4}$$

where $\mathbf{D}$ is a constant fourth order constitutive tensor, also called the *tangent(elastic) stiffness tensor*, which depends on the Green's strain. Furthermore, the strain-displacement relation can be written in an informative and compact form given by

$$\mathbf{E} = \left[\nabla\mathbf{u} + \frac{1}{2}\nabla\mathbf{u}\cdot(\nabla\mathbf{u})^T\right]. \tag{5.5}$$

Here, the difference between the formulation for small-deformation and large-deformation is clearly evident through the second non-linear term.

The strain-displacement relation in (5.5) has been based on three-dimensional tetrahedral elements as shown in Figure 5.1. This is a four-node tetrahedra finite element, where its topology is such that each node consists of three degrees of freedom for translational displacements, u_x,u_y,u_z. Hence, rotations are not considered. Here, the unknown displacements, $\mathbf{u}$, are computed by using linear approximation between the nodal points in each element and the strains, in turn, are computed by differentiating the shape functions, $\mathbf{N}_i$, which enable interpolation of polynomials within the element according to

$$\mathbf{u}\left(x, y, z\right) = \sum_{i}^{4} \mathbf{N}_i^e \mathbf{u}_i. \tag{5.6}$$

Indeed, the shape function belonging to a specific node has a universal property, which states that the shape functions is zero at all nodes which it doesn't belong to,

$$N_i^e = \begin{cases} 1 & \text{at nodal point } i \\ 0 & \text{at all other nodal points.} \end{cases} \tag{5.7}$$

Moreover, the strain components are all evaluated by performing a full integration by using four point Gauss integration formula. The corresponding weights, w_i, and Gaussian coordinates, ξ_i, can be found in references [79, 80].

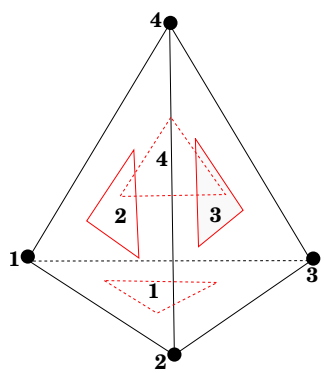

Figure 5.1: Linear tetrahedral element, definition and node numbering.

5.2 Numerical Treatment of Solids

This section reports briefly the Finite Element discretization technique employed to the momentum equations of the dynamically loaded flexible cantilever beam. Also, the utilized time-marching scheme is presented and shortly discussed.

5.2.1 Non-linear Finite Element Formulation

The finite element (FE) formulation for geometrical non-linear problems suitable for large deformations and small strains, corresponding to the virtual work expression in (5.3) can be approximated as

$$\mathbf{c}^T \left(\int_v \rho \mathbf{N}^T \mathbf{N} \ddot{\mathbf{a}} \, dv + \int_v \mathbf{B}^T \mathbf{S} \, dv - \int_s \mathbf{N}^T \mathbf{t} \, ds - \int_v \rho \mathbf{N}^T \mathbf{b} \, dv \right) = 0, \quad (5.8)$$

where the displacement field, $\mathbf{u}$, and the arbitrary virtual displacements, $\delta\mathbf{u}$, are approximated by the shape functions, $\mathbf{N}$, according to

$$\mathbf{u}\left(\mathbf{x}, \mathbf{t}\right) = \mathbf{N}\left(\mathbf{x}\right) \mathbf{a}\left(\mathbf{t}\right), \quad \delta\mathbf{u}\left(\mathbf{x}, \mathbf{t}\right) = \mathbf{N}\left(\mathbf{x}\right) \mathbf{c}\left(\mathbf{t}\right), \quad (5.9)$$

where $\mathbf{a}$ is the nodal displacement vector. Evidently, (5.8) describes the linear momentum of the system in a weighted sense for which the system of equations has to be solved for. This statement gives that (5.8) can be written as

$$\mathbf{M}\ddot{\mathbf{a}} + \mathbf{f}_{int} - \mathbf{f}_{ext} = \mathbf{0}, \quad (5.10)$$

where the mass matrix, $\mathbf{M}$, is defined as

$$\mathbf{M} = \int \rho \mathbf{N}^T \mathbf{N} \ddot{\mathbf{a}} \, dv, \quad (5.11)$$

and

$$\mathbf{f}_{int} = \int_v \mathbf{B}^T \mathbf{S} \, dv, \qquad \mathbf{f}_{ext} = \int_s \mathbf{N}^T \mathbf{t} \, ds - \int_v \rho \mathbf{N}^T \mathbf{b} \, dv. \quad (5.12)$$

Non-linear Dynamic Loading

Two general classes of algorithms for dynamic problems exist, implicit and explicit. *Explicit* algorithms [81] tend to be inexpensive in their solution procedure per time step since the solution may be advanced without storing a matrix for solving a system of equations and therefore do not require large storage of data. However, numerical stability requirements restricts the problem to small time steps. On the other hand, *implicit* algorithms are numerically stable and, hence, permit for larger time steps. But, the profit in numerical stability is somehow lost in numerical efficiency due to high storage requirements of data since a matrix system has to be solved per time step in order to advance the solution.

In this thesis the implicit method has been chosen for stability reasons. Especially, the long duration character of the oscillating cantilever beam is well suited for implicit formulation of the equation of motion, where the response dynamics is mostly controlled by the low frequency modes.

Dynamic problems with essential non-linearities are mostly solved by time integration of the non-linear equations of motions. Traditionally these problems have been solved by the so-called collocation-type methods, where the equation of motion is matched at selected points with suitable assumptions regarding the relation between displacement, velocity and acceleration, see e.g. [76]. In implicit methods, equilibrium conditions are considered at the same time step for which the solution is sought. If the solution is known at time t and the unknown displacements are sought at time $t+\triangle t$, then the discretized version of (5.10) at time $t+\triangle t$ becomes (by adding damping into the system) as follows:

$$\mathbf{M}\ddot{\mathbf{a}}_{t+\triangle t} + \mathbf{C}\dot{\mathbf{a}}_{t+\triangle t} + \mathbf{f}^{int}\left(\mathbf{a}\right)_{t+\triangle t} = \mathbf{f}^{ext}_{t+\triangle t}. \tag{5.13}$$

This is achieved by predicting the nodal velocity, $\dot{\mathbf{a}}$, and, acceleration, $\ddot{\mathbf{a}}$, with an appropriate method, while the displacement, $\mathbf{a}$, is solved for in the solution of the equations of motion. There exist several different numerical techniques to achieve this, such as Newmark-beta method, Crank Nicholson method, two-point Backward Euler and three-point Backward Euler method, to name a few.

In this thesis, the three-point Backward Euler method, e.g. [82], has been used for the time-marching procedure and is based on the following assumptions for the discretized displacement and velocity:

$$\begin{aligned} \mathbf{a}_{t+\triangle t} &= \mathbf{a}_t + \triangle t\, \dot{\mathbf{a}}_t + (\triangle t)^2 / 2\, \ddot{\mathbf{a}}_{t+\triangle t}, \\ \dot{\mathbf{a}}_{t+\triangle t} &= -4/(2\triangle t)\, \mathbf{a}_t + 3/(2\triangle t)\, \mathbf{a}_{t+\triangle t} + 1/(2\triangle t)\, \mathbf{a}_{t-\triangle t}. \end{aligned} \tag{5.14}$$

Moreover, the internal force vector in (5.13), $\mathbf{f}^{int}(\mathbf{a})_{t+\triangle t}$, is a non-linear function of the displacement, $\mathbf{a}$, corresponding to the stress-strain relation at time $t+\triangle t$. Nevertheless, the internal force vector needs to be expressed in terms of the previous time step, t, in order to be compatible for implicit time integration. Hence, the internal forces are predicted by linearization utilizing the tangent stiffness method as:

$$\mathbf{f}^{int}(\mathbf{a})_{t+\triangle t} = \mathbf{f}^{int}(\mathbf{a})_t + \mathbf{K}(\mathbf{a})_t\, \delta\mathbf{a}, \tag{5.15}$$

where, $\mathbf{K}(\mathbf{a})_t = \partial\mathbf{f}^{int}/\partial\mathbf{a}_t$, is the tangential stiffness matrix evaluated at time, t, and , $\delta\mathbf{a} = \mathbf{a}_{t+\triangle t} - \mathbf{a}_t$, is the incremental displacement between two time steps in the upwind sense.

In conclusion, the solution to (5.13), as a function of the unknown displacement increment, obtains a linearized character by expressing the discretized velocity and acceleration as a function of the displacement increment via (5.14) and by utilizing the linearized internal force vector defined in (5.15), which as a sum up yields:

$$\mathbf{M}\left[b_0\, \delta\mathbf{a} - b_2\, \dot{\mathbf{a}}_t\right] + \mathbf{C}\left[b_1\, \delta\mathbf{a} - b_3\, \delta\mathbf{a}_-\right] + \mathbf{f}^{int}(\mathbf{a})_t + \mathbf{K}(\mathbf{a})_t\, \delta\mathbf{a} = \mathbf{f}^{ext}_{t+\triangle t}, \tag{5.16}$$

where the previous incremental displacement is defined as, $\delta\mathbf{a}_- = \mathbf{a}_t - \mathbf{a}_{t-\triangle t}$, and the coefficients are ,$b_0 = 2/(\triangle t)^2$, $b_1 = 3/(2\triangle t)$, $b_2 = 2/(\triangle t)$, and $b_3 = 1/(2\triangle t)$.

In general, the solution to (5.16) yields an approximate displacement increment, $\delta\mathbf{a}$. To avoid the development of numerical errors and to improve the accuracy of the solution, a Newton-Raphson iteration scheme is applied within each time step. The details of the solution procedure for the non-linear problem using the three-point Backward Euler algorithm are outlined in Table 1 [82].

A side note; although the damping matrix, $\mathbf{C}$ in (5.16) is explicitly shown it is not numerically considered in the simulations in order to allow for worst case scenarios in the structural dynamics. However, there exist an alternative to model it as a Rayleigh damping $\mathbf{C} = \alpha\mathbf{M} + \beta\mathbf{K}$.

Algorithm 1 Non-linear (dynamic) solution procedure using three-point Backward Euler method.

1. Initialize initial conditions $\mathbf{a}_0, \mathbf{a}_1, \mathbf{a}_2, \mathbf{a}_6$
2. Calculate constants
$b_0 = \frac{2}{(\triangle t)^2}; \quad b_1 = \frac{3}{(2\triangle t)}; \quad b_2 = \frac{2}{(\triangle t)}; \quad b_3 = \frac{1}{(2\triangle t)};$
3. Form the matrices $\mathbf{M}$, $\mathbf{C}$ and $\mathbf{K}_t$.
4. Form the effective stiffness matrix, assuming linear behaviour
$$\mathbf{K}_t^\star = b_0\mathbf{M} + b_1\mathbf{C} + \mathbf{K}_t;$$
5. If tangent stiffness method is used, optionally update $\mathbf{K}_t$
$$\mathbf{K}_t = \int_v \mathbf{B}^T\mathbf{D}\mathbf{B}\, dv;$$
6. Form the effective load vector
$$\mathbf{f}_{t+\triangle t}^\star = \mathbf{f}_{t+\triangle t}^{ext} - \mathbf{f}_{t+\triangle t}^{int} + \mathbf{M}\,(b_2\dot{\mathbf{a}}_t) + \mathbf{C}\,(b_3\,\delta\mathbf{a}_-);$$
7. Solve for initial displacement increment
$$\delta\mathbf{a}^0 = (\mathbf{K}_t^\star)^{-1}\,\mathbf{f}_{t+\triangle t}^\star;$$
8. Iterate for dynamic equilibrium, $i = 0$:
   (a) $i = i + 1$
   (b) Evaluate acceleration, velocity and displacements using (5.14)
   (c) Evaluate the residual force
$$\mathbf{R}_{t+\triangle t}^{i-1} = \mathbf{F}_{t+\triangle t}^{ext} - \left(\mathbf{M}\ddot{\mathbf{a}}_{t+\triangle t}^{i-1} + \mathbf{C}\dot{\mathbf{a}}_{t+\triangle t}^{i-1} + \mathbf{f}^{int}\,(\mathbf{a})_{t+\triangle t}^{i-1}\right);$$
   (d) Solve for the corrected displacement increments
$$\triangle\mathbf{a}^i = (\mathbf{K}_t^\star)^{-1}\,\mathbf{R}_{t+\triangle t}^{i-1};$$
   (e) Evaluate the corrected displacement increments
$$\delta\mathbf{a}^i = \delta\mathbf{a}^{i-1} + \triangle\mathbf{a}^i;$$
   (f) Check convergence in terms of residual norm, relative displacement norm, etc.
   (g) Return to step 5 to process the next time step, $\triangle t$.

Non-linear Static Loading

A similar approach as for the dynamic loading procedure can be established for non-linear static structural problems. Following Ristinmaa and Ljung [83], the initial problem to be solved is again (5.10), with the difference that the dynamic term is neglected and instead static equilibrium equations must be fulfilled, i.e.

$$\mathbf{R}\left(\mathbf{a}\right) \equiv \mathbf{f}^{int}\left(\mathbf{a}\right) - \mathbf{f}^{ext} = \mathbf{0}, \tag{5.17}$$

where it is assumed that the external loading does not depend on the displacements. To obtain an iterative format based on the Newton-Raphson method a Taylor expansion of (5.17) around an equilibrium state is made. It is assumed that the state $(\mathbf{a} + d\mathbf{a})$ is in equilibrium where $d\mathbf{a}$ denotes small increment in nodal displacements. A truncated Taylor series expansion of (5.17) yields

$$\mathbf{R}\left(\mathbf{a} + d\mathbf{a}\right) = \mathbf{R}\left(\mathbf{a}\right) + d\mathbf{R}\left(\mathbf{a}\right), \tag{5.18}$$

where $\mathbf{R}\left(\mathbf{a} + d\mathbf{a}\right) = \mathbf{0}$ at equilibrium. It should be noted that the differential in the Taylor series expansion in (5.18) is usually called *directional derivative* and is equal to

$$d\mathbf{R} = d\mathbf{f}_{int} = \int_v d\mathbf{B}^T \mathbf{S} dv + \int_v \mathbf{B}^T d\mathbf{S} dv. \tag{5.19}$$

A further simplification of (5.18), by using (5.19) yields

$$\mathbf{0} = \mathbf{R}(\mathbf{a}) + \mathbf{K}\, d(\mathbf{a}), \tag{5.20}$$

where the tangential stiffness matrix is defined as

$$\mathbf{K} = \int_v \mathbf{B}^T \mathbf{D} \mathbf{B} dv + \int_v \mathbf{H}^T \mathbf{R} \mathbf{H} dv. \tag{5.21}$$

The first term in (5.21) is related to the material model, whereas the second is associated with non-linear geometry changes. A summary of the solution procedure for non-linear static problem, based on load control method (displacement control is another choice), is shown in Table 2.

Algorithm 2 Total Lagrangian formulation for non-linear Static Loading.

1. Evaluate initial load increment
$$\mathbf{f}_n^{ext} = \mathbf{f}_{n-1}^{ext} + \triangle \mathbf{f}_n^{ext}$$
2. Form and optionally update the stiffness matrix
$$\mathbf{K}_n = \int_v \mathbf{B}^T \mathbf{D} \mathbf{B} dv + \int_v \mathbf{H}^T \mathbf{R} \mathbf{H} dv$$
3. Solve for initial displacement increment
$$\delta \mathbf{a}_n^0 = (\mathbf{K}_n)^{-1} \mathbf{R}_n$$
4. Iterate for dynamic equilibrium, $i = 0$:
   (a) $i = i + 1$
   (b) Evaluate approximation to the displacement
   $$\mathbf{a}_n^{i-1} = \mathbf{a}_n + \delta \mathbf{a}_n^{i-1}$$
   (c) Evaluate the residual force
   $$\mathbf{R}_n^{i-1} = \mathbf{f}_n^{ext} - \mathbf{f}^{int} (\mathbf{a})_n^{i-1};$$
   (d) Solve for the corrected displacement increments
   $$\triangle \mathbf{a}_n^i = (\mathbf{K}_n^\star)^{-1} \mathbf{R}_n^{i-1};$$
   (e) Evaluate the corrected displacement increments
   $$\delta \mathbf{a}_n^i = \delta \mathbf{a}_n^{i-1} + \triangle \mathbf{a}_n^i;$$
   (f) Check convergence in terms of residual norm, relative displacement norm, etc.
   (g) Return to step 1 to process the next loading step, n.

CHAPTER 6

Two-way FSI Methodology

This chapter describes, briefly, the methodologies in the treatment of the interaction between fluid and solid domains for both flexible and rigid bodies firstly, from a general perspective, and thereafter, the specifically utilized techniques in each case are concisely outlined.

6.1 Interface Treatment and Flexible Cantilever

Computational fluid-structure interaction (FSI) emerged in the early 1960's in conjunction with the need to deal with linear problems in acoustics, vibrations and flutter [84]. The first attempt to tackle the multi-physical problem was using formulations in the frequency domain due to the limited computer capacity available [85]. Time-domain FSI had a breakthrough first in the 1970's as non-linear properties of the fluid and structure become more highlighted within the FSI-context. For (partitioned) fluid-structure interaction, the Finite Element Method (FEM) has been the natural choice to discretize the structural problem whereas there is no universal methodology for the fluid field. Instead, the choice of method in the fluid discipline is to some extent problem-dependent. Nevertheless, commonly used discretization techniques rely, among oth-

ers, on the Finite Differences (FD) and Finite Volumes (FV) approaches which were discussed in chapter 3.2.1 and 3.2.2, respectively. Within the FSI-context, factors such as time-marching methods and, in particular, treatment of fluid-solid interface arise as issues of complexity common for both fields. Interface treatment and its proceedings deserve a particular emphasis since this is one of the key parts of the partitioned FSI coupling procedure.

In this thesis, the FSI-methodology for the flexible cantilever beam case relies on the partitioned approach which retains separate domains for fluid (Ω_F) and solid (Ω_S) fields. In fact, the fluid and solid domains are unionly integrated by considering the respective boundaries of fluid (Γ_F) and solid (Γ_S), and the mutual interface boundary, ($\Gamma_{F/S}$). These boundaries are shown in Figure 6.1 together with an illustration of a typical time-marching scheme.

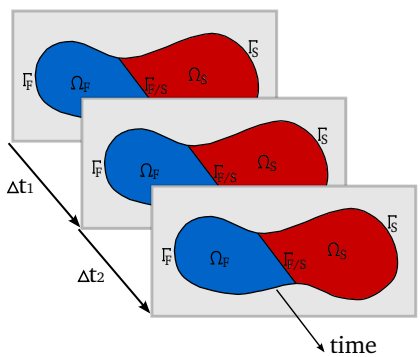

Figure 6.1: Fluid-structure interaction problem subdivided into fluid and solid domains with inherent boundaries.

Proper treatment of fluid and solid interfaces, ($\Gamma_{F/S}$), can be accomplished by considering certain relevant parameters. The first parameter to consider is whether the fluid and solid meshes are mutually in a *matching* or *non-matching* state. Traditionally, it is claimed that a denser fluid mesh is required to resolve the small scales in the fluid flow and thus, a coarse mesh for the solid domain is seen as satisfactory. This has been the general approach to treat fluid-solid interfaces within the FSI com-

munity. Moreover, the process of data transfer from fluid to solid, and vice versa, at the fluid-solid 'wet' interface is not straight-forward and requires a thoroughly consideration for non-matching interfaces. The data transfer can be summarized in the following scheme:

F $\Rightarrow$ **S** Interface fluid stresses/pressures are transferred to structural nodes.
F $\Leftarrow$ **S** Structural displacements are transferred as interface fluid-particle velocities.

A second consideration would be based upon the technique used to communicate the exchange of data transfer between the fluid and solid domain. Felippa et al. [84] discusses three interface treatment prototypes. The first one, being the oldest and easiest to implement, is the Direct Force-Motion Transfer (DFMT) scheme, where the exchange data is transferred directly. Depending on the fluid problem necessary interpolation routines can be employed. In the Mortar scheme, the interface freedoms are linked through Lagrange multipliers instead. The multipliers are distributed (delta) functions interpretable as surface tractions. The last scheme, named Localized Lagrange Multipliers (LLM), uses a kinematic 'frame' between the fluid and solid domain to transfer the exchange data.

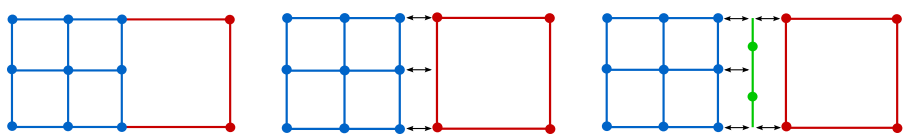

Figure 6.2: Sketches for realizations of three interface treatment prototypes. Left; DFMT, Middle; Mortar, Right; LLM.

Independent of which variant of 'gluing' technique is preferred, matching or non-matching, there are critical aspects that needs to be considered ahead any interface treatment method is utilized:

- Method flexibility; Both matching and non-matching meshes should be optional.

- Flux consistency; Mass and momentum should be considered over the interface.
- Energy conservation; Energy should not be produced or dissipated at the interface.
- Time stepping stability and accuracy; Should be independent on the choice of interface treatment (applicable for partitioned time stepping).
- Computational flexibility; Handle non-linear problems and parallelization friendly.

The handling of mesh motion arises as an auxiliary component that needs to be considered when developing interface treatment methods in fluid-structure interaction simulations. Traditionally, this has been done using an Eulerian (fixed) formulation for the fluid while a Lagrangian formulation has been used for the structural part. The Arbitrary Lagrangian-Eulerian (ALE) formulation, combining both the Eulerian and Lagrangian formulation, has been the approach used for deformation of the fluid mesh in response to the structural deformations [86]. Alternatives to the ALE approach include immersed boundary method and fictitious domain method among others. These methods to some degree involve the more general Lagrange multiplier approach and use fixed fluid mesh. The advantage of the ALE approach over fixed-mesh alternatives is the ability to maintain high-quality meshes near the structure's interface, resulting in more accurate solutions on the fluid side [87]. Nevertheless, with ALE a further non-linearity is introduced into the FSI system of equations, as a new equation for the fluid domain motion is required, which also contributes to the overall computational time.

6.1.1 Explicit Coupling

Conventional sequential staggered (CSS) schemes are the most basic and popular partitioned (explicit) algorithms for solving FSI problems [88]. The procedure involves first a *p*rediction of the structure's motion (${}^{p}\mathbf{u}_s^{n+1}$), solution of the (e.g. ALE) fluid domain in order to compute the

(normal and shear) stresses acting on the fluid interface ($\boldsymbol{\sigma}_f^{n+1}$), extraction for (viscous and pressure) forces acting on the structure, ($\boldsymbol{\sigma}_s^{n+1}$) and, finally, solution for the new structure displacement ($\mathbf{u}_s^{n+1}$). The principals of the CSS scheme is shown in Figure 6.3. Since no convergence is checked between the predicted and computed structural displacements at the end of a time-step this method is not able to guarantee a matching of the boundary conditions at the interface. As a result, destabilizing effects may be introduced through interface discretization [89]. Moreover, due to a time-lag between the structural and fluid computations, the CSS schemes are at most 1st order accurate in time at the boundary interface [89].

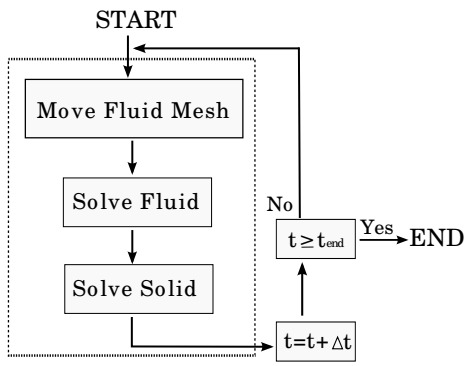

Figure 6.3: Conventional sequential staggered (CSS) approach.

Despite the great simplicity and low computational cost of explicit partitioned schemes they suffer from two major problems, (i); the numerical instability of the coupling scheme caused by energy production along the interface due to time lag [90, 89] and (ii); lost of temporal accuracy of the coupled analysis.

Jaiman et al. [91] presented a novel staggered coupling method which improves the stability and accuracy for explicitly coupled staggered fluid and structure problems, named the Combined Interface Boundary Condition (CIBC) method. Here, the relative physical and geometrical properties at the fluid and solid interface, not considered for the CSS procedure and otherwise leading to artificial energy production, are taken account

for by introducing high-order interface corrections. More specifically, the CIBC method requires a coupling parameter for combining the spatial and temporal derivatives of velocity and momentum fluxes by constructing PDEs from the interface continuity conditions.

Despite the presented robustness of the CIBC scheme by Jaiman et al. [91] there are challenging questions concerning practical applications of such methods. One such is to find suitable values for the coupling parameter. Furthermore, the validity of these solution procedures is not verified for applications when the densities of the two sub-domains are in the same range, as is the case in hydroelasticity simulations.

As was mentioned in the Introduction, an implicit coupling scheme has been chosen for the work in this thesis accounting for the added-mass effect (and the instabilities caused by it) and hence, the solution of both fluid and structural problems are repeated until dynamic equilibrium is achieved.

6.1.2 Implicit Coupling Strategy

Relaxation techniques usually serve as a conventional approach on the treatment of interface displacement of the fluid mesh, $\mathbf{u}_f$, in implicitly coupled FSI problems. The relaxation used in this thesis is established by Aitken relaxation [92]. The Aitken relaxation factor, ω, is defined in (6.1), where i is the sub-iteration number and $\mathbf{u}_s$ is the structural displacement at the interface, is applied to the displacement of the fluid interface according to $\mathbf{u}_f^i = (1-\omega_i)\mathbf{u}_f^{i-1} + \omega_i \mathbf{u}_s^{i-1}$. Prior to the relaxation, however, the fluid mesh interface is moved according to a second order extrapolation based on Taylor expansion.

$$\omega^i = -\omega^{i-1} \frac{(\mathbf{u}_s^{i-1} - \mathbf{u}_f^{i-1}) \cdot ((\mathbf{u}_s^{i-1} - \mathbf{u}_f^{i-1}) - (\mathbf{u}_s^{i-2} - \mathbf{u}_f^{i-2}))}{\|(\mathbf{u}_s^{i-1} - \mathbf{u}_f^{i-1}) - (\mathbf{u}_s^{i-2} - \mathbf{u}_f^{i-2})\|_2^2}, i = 2, 3, 4, ... \tag{6.1}$$

The fluid-structure interaction procedure is accomplished by communication of fluid stress information from the flow to the structure and structural displacement from the structure to the fluid domain. This convention is obviously a prerequisite for stability reasons and thus the reversing, i.e. imposing stress boundary condition on the fluid and velocity on the solid is avoided, as discussed by Bathe and Zhang [93].

This leads to the following requirements at the fluid/solid interface corresponding to no-slip and compatibility conditions;

$$\mathbf{v}^m = \frac{d\mathbf{u}}{dt} \tag{6.2}$$

$$\boldsymbol{\sigma}^s \cdot \mathbf{n} = \boldsymbol{\sigma}^f \cdot \mathbf{n}, \tag{6.3}$$

where, $\mathbf{n}$, is the unit normal on the interface, $\mathbf{v}^m$, the mesh velocity associated with the ALE formulation and $\boldsymbol{\sigma}$ denotes the stress acting on either of the sub-domains.

In Figure 6.4, a schematic drawing of the implicit coupling is shown. The procedure could be described as follows; First the fluid velocities and pressure is solved using a suitable solver (PISO in this case). Next the pressure and viscous forces asserted on the solid are transferred from the fluid to the structural solver to act as a boundary condition. Next, the structural displacements is solved for, which in turn, become boundary conditions for the moving mesh. Subsequently the convergence criterion is evaluated,$\|(\mathbf{u}_f^{i+1} - \mathbf{u}_s^{i+1})\|_2 \ /max(\|\mathbf{u}_f^0 - \mathbf{u}_s^0\|_2) < \text{Tol}$, where Tol is the relative tolerance and the max indicates that the largest norm up till time t is used. Next, assuming that the first sub-iteration ($i = 0$) is considered, the sub-iteration number is increased by one, $i++$, and the Aitken relaxation step is performed. Note that the first relaxation factor, ω^1, needs to be either specified by the user or computed in some other way. In this work the first relaxation factor in the first time-step is user-defined whereas in the following time-steps the last relaxation factor from the previous time-step is used. The new fluid interface displacement, $\mathbf{u}_f^1$, has now been estimated and the fluid mesh is to be moved. Next up is solving the flow equations and after that the structural equations. When this is done the convergence criterion is once again evaluated. Assuming that the convergence criterion is fulfilled the iteration now goes to the next time-step and if the total time exceeds the end time, t_{end}, the simulation is stopped.

Interface Communication

An introductory description of the interface treatment applicable to non-matching interfaces was outlined in section 6.1. Non-matching in-

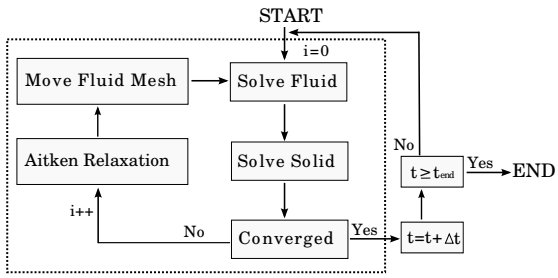

Figure 6.4: Partitioned approach for implicitly coupled FSI with relaxation technique.

terfaces can be desired due to reasons such as different discretization techniques for the subdomains (finite volumes vs. finite elements), different types of grids and different grid resolutions. Consequently, a grid-to-grid data interpolation and transfer becomes unavoidable. However, transfer of data in combinations with interpolation routines not only are time-demanding operations but also require extra care in the overall procedure.

It is the lack of energy conservation at the fluid and solid interface that forms an essential feature from a physical point of view when considering different coupling schemes that utilize non-matching interface approach. This effect is concerned with integral quantities such as the (viscous and pressure) forces. Lesoinne et al. [94] describe the conservative interpolation approach for the transfer of forces which ensures that the resultant loads on both grids are exactly the same. It is a technique that, first, integrates the fluid stresses that resides on the fluid and solid interface and afterwards, distributes the resultant forces to the structure by means of regular interpolation routine, as demonstrated in Campbell and Breuer [13, 95]. In particular, Campbell, discusses the importance of the quantities to be transfered; a transfer of the stress values (instead) to the structure face and *then* integrating the stress to compute the forces gives rise to an inconsistency in the load balance between the two subdomains.

To avoid the disadvantages associated with interpolation matching grids on the fluid and solid sides have been used throughout this work.

There are also theoretical results proving stability when using matching interfaces, however, it should be noted that the results are limited to FEM in theory.

6.2 Moving Boundaries and Rigid Cylinder

Historically, various computational techniques have been utilized in order to (numerically) consider the solid domain, i.e. the rigid circular cylinder, in the fluid-flow simulations.

Stationary bodies are normally described by using body fitted structured or unstructured grids, where the boundaries become well defined and the specification of the boundary conditions are straight forward. Within finite differences a disadvantage of these methods is the required co-ordinate transformation which is a time-demanding cost in terms of computational operations.

Geometric complexity in combination with moving boundaries further increase the computational challenges, since these properties require regeneration or deformation of the grid as the boundary is moved. Deforming grids, for example, follow the boundary motion and preserve the shape at the same time. The main drawback is that re-meshing is required when the grid is too deformed. This leads to an interpolation process between the old and the new grid.

An alternative to the above-mentioned approaches is to use overlapping grids. This technique allows the main region of the problem to be divided into subregions in the sense that a union of all grids cover the total domain of interest. The required boundary conditions on the object is set quite easily, whereas the interpolation procedure between different grids may cause a loss of accuracy.

In the Arbitrary Lagrangian Eulerian (ALE) method, the boundary between the fluid and solid is well defined as for structured/unstructured grids. However, the method has difficulties in the handling of large deformations and rotations where the fluid mesh elements may become distorted resulting in reduced accuracy. As a result, solution strategies for engineering CFD problems need to be able to cope with flow complexity but at the same time retain the numerical accuracy and efficiency of the simulations performed on various kind of grids.

Fixed Cartesian grid is an example of methods where the advantage of easy implementation of higher-order discretization are preserved. Furthermore, there is no need for mesh regeneration. However, representing complex solid boundaries on a Cartesian grid requires additional treatment. Immersed Boundary (IB) methods is a numerical approach for relating the fluid- and solid domains on Cartesian grids. The idea is that the fluid domain is represented by a fixed mesh, wherein the solid domain is represented by momentum sources enforcing the required boundary condition.

The use of momentum sources to describe boundaries, also referred to as 'virtual boundary' methods, can be traced back to the pioneering works by Peskin [96] who proposed an IB method for studying the flow of blood past an elastic (2D) heart valve computed with a finite difference method. Goldstein et al. [97] developed a pseudo-spectral method related to Peskin's [96] immersed boundary approach where they used a feedback scheme (similar to PI-regulator) based on control system theory in order to compute the force field on the boundary. Mohd-Yusof [98] derived an alternative formulation (to the one presented by Goldstein et al. [97]) of the forcing. This is also an pseudo-spectral code, however, it does not suffer from the stability issues of the discrete-time equations when the immersed boundary technique is combined with spectral methods. Further, Fadlun et al. [99] compared the forcing methods by Goldstein et al. [97] and Mohd-Yusof [98] by using a second order finite difference scheme, and found that the latter is more efficient due to a higher achieved CFL-number without loosing stability.

Young et al. [100] developed a numerical model for computing the flow and heat transfer problems with moving and complex boundaries. The technique here, followed the immersed boundary method in the ALE framework (to reduce numerical diffusion near the immersed boundary) with direct forcing formulation proposed by Mohd-Yusof [98]. The major drawback of this method is the relatively low accuracy proximate to the boundary due to the spreading of the forcing function or the interpolation scheme.

Kim and Peskin [101] have applied the immersed boundary (IB) method to study fluid-structure interaction in $3D$ parachute aerodynamics. They used the penalty immersed boundary (pIB) method in order

to take into account the inertial and gravitational effects of boundary mass in an immersed boundary computation. It was shown that the IB methodology is capable of simulating the detailed structure of an immersed boundary, its ability to handle large deformations without regridding and in particular, its ability to handle collisions without the use of any special collision detection algorithm.

6.2.1 Boundary Conditions

As was mentioned above the idea of using IB-method is to model the rigid body, which represents a discontinuity in the flow field, by introducing momentum source terms into the flow field (momentum equation (3.11)). The main idea is based on Newton's third law of action- and reaction between the fluid and solid domains. Consider a boundary in the form of a closed surface Γ in a domain Ω with the parametrization of the surface given by $X_i(s_i, t)$, then the force in the flow field can be written as

$$\Phi_i\left(x_j, t\right) = \int\int\int_{\Omega} F_i\left(s_j, t\right) \delta\left(x_j - X_j\right) dx_1 dx_2 dx_3, \tag{6.4}$$

where F_i is the force on the surface and δ is the three dimensional Dirac delta function. Hence, the source terms will only be non-zero at the location of the boundary. However, discretizing the computational domain using a Cartesian grid will in the general case lead to that the nodes on the grid will not coincide with the location of the surface of a body of arbitrary shape. The presence of the boundary must therefore be represented by source terms in positions away from the actual boundary location. This can be achieved in different ways, for example by approximating the Dirac function by a normalized Gaussian distribution [102] or by assuming a certain distribution of the velocity field normal to the boundary [103]. Here, a brief description of the numerical procedure developed by Revstedt and Fuchs [104] is presented:

1. *Discretization of the boundary surface:* The $(2D)$ boundary surface is discretized in such a way that the node distance is somewhat smaller than the $(3D)$ fluid-mesh.

2. *Applying the correct boundary conditions:* The desired boundary condition on the surface nodes is satisfied by applying the no-slip condition. This implies that the velocity on the surface nodes should vanish or at least approach zero (providing that the boundary is fixed). Since the fluid-mesh and surface-mesh nodes do not in general coincide the appropriate variables (in this case the three velocity components v_i^f) need to be determined on the surface mesh. Revstedt and Fuchs [104] investigated two methods in order to determine the velocity at the surface nodes, namely: Lagrange interpolation and Gaussian weighted averaging. They found that the Gaussian method gives faster convergence and was less computationally expensive than the Lagrangian method. For this reason, the Gaussian interpolation scheme for the boundary velocity v_i^f has been used

$$v_i^f = \int_{\xi-2}^{\xi+2} \int_{\kappa-2}^{\kappa+2} \int_{\varpi-2}^{\varpi+2} v_i G_F \, d\xi \, d\kappa \, d\varpi, \tag{6.5}$$

where ξ_j is the boundary position normalized with the mesh spacing and G_F is a Gaussian distribution function

$$G_F = \frac{1}{\left(\varsigma\sqrt{2\pi}\right)^3} e^{\left(-\xi^2+\kappa^2+\varpi^2\right)/2\varsigma^2}, \tag{6.6}$$

where ς is the variance of the Gaussian distribution function.

3. *Determining the defect to the surface force:* The surface force contributions are estimated in order to satisfy the boundary condition, which for a solid object implies that v_i^f vanishes. This is achieved by calculating the velocity defect, which is the difference between calculated velocity on the boundary v_i^f, and the prescribed boundary condition v_i^b

$$F_i^n = F_i^{n-1} + \left(\alpha \frac{v_{def}}{h^2}\right)^n, \tag{6.7}$$

where F_i is the surface forces, α is a relaxation parameter (proportional to Reynolds number), $v_{def} = v_i^f - v_i^b$ is the velocity defect, h

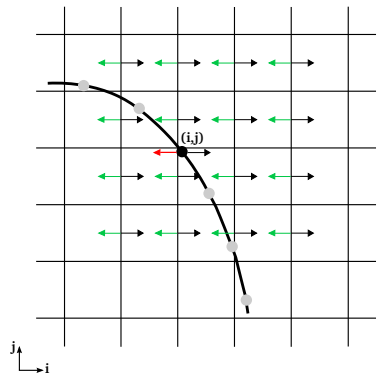

Figure 6.5: A schematics of the Immersed Boundary mesh crossing the fluid mesh.

is the node distance of the computational grid and n is the iteration number within one time step. Figure 6.5 illustrates the procedure of estimating the velocity defect.

4. *Distribution of the surface forces:* The final step of the algorithm is the distribution of the surface forces F_i to the computational domain. However, it should be mentioned that the boundary is represented by a discontinuity which mathematically can be described by a Dirac δ-function with the following properties

$$\int_{-\infty}^{\infty} \delta(x - x_i)\, dx \;=\; 1, \quad \delta(x - x_i) = \begin{cases} \infty, & x = x_i, \\ 0, & x \neq x_i. \end{cases} \tag{6.8}$$

Nevertheless, this cannot be represented on a discretized grid and instead the Gaussian distribution in (6.6) is used in order to transfer the forces back to the computational grid and the source terms can then be written as

$$\phi_i = \frac{1}{N} \sum_{i=1}^{N} G_F\, F_i, \tag{6.9}$$

where N is the number of contributions from the surface to certain grid point.

The above method of estimating the the source terms has been used in preliminary stage of this thesis work [105, 106]. In the study of PAPER4 a recent extension of the virtual boundary method, with improved numerical efficiency and accuracy, developed by Duwig and Revstedt (not yet published) was used. In this method the following expression is employed for the discretized source terms:

$$\overline{\Phi_i} = C_1 \frac{(v_i' - v_i)}{\triangle t} e^{-C_2 d^2}, \tag{6.10}$$

where C_1 and C_2 are positive constants, v_i' is the target velocity of the solid surface and d is a positive function which should increase rapidly with increasing distance from the solid boundary. If the body is considered as thick (i.e. spans over several computational nodes) d will be set to zero inside the body and to a large positive value, typically 10^6, far away from the body. In computational cells cut by the surface mesh d is set as a function of the normal distance from the computational node to the virtual surface. This strategy is also employed for bodies of sub-grid thickness. Hence, in this method the surface mesh is only used to keep track of the surface position and for calculating the normal directions of the surface. No variables are calculated on the surface mesh and hence there is no need for distribution of the force from it. Unpublished results by Duwig and Revstedt indicate that this kind of strategy gives a second order accuracy of the boundary formulation.

Solving the Equation of Motion for a Rigid Cylinder

The equation of motion of an elastically mounted cylinder, may be written as

$$m\frac{d^2x}{dt^2} + b\frac{dx}{dt} + kx = F_x, \tag{6.11}$$

where F_x is the instantaneous lift force and x is the transverse displacement. It is common practice to express (6.11) in a non-dimensional form using the structural quantities

$$x^\star = \frac{x}{D}, \quad t^\star = t\omega_N, \quad \zeta = \frac{b}{2\sqrt{km}}, \tag{6.12}$$

for the mass m, damping b, and spring stiffness k, which leads to the following form of the equation of motion, (6.11):

$$\frac{d^2x^\star}{dt^{\star 2}} + 2\zeta\frac{dx^\star}{dt^\star} + x^\star = C_x n V^{\star 2}, \tag{6.13}$$

where $C_x = 2F_x/(\rho V_\infty^2 DL)$ is the transverse force coefficient and $n = \rho D^2 L/(2m)$ is a mass parameter. In this case, the structural parameters defining the behaviour of the system are ζ, n and $V^\star$. It can be seen that, $\omega_N = 2\pi f_N$ is used in the scaling of velocity, which leads to the reduced velocity, $V^\star$. A disadvantage of this kind of scaling is that at zero mass $m = 0$, or zero stiffness $k = 0$, it will yield an infinite damping coefficient, ζ. To avoid this, one may instead use the flow parameters to non-dimensionalize the equation of motion, cf. Shiels et al. [53]. This approach leads to the following non-dimensional form of the cylinder equation of motion

$$m^\star\frac{d^2x^\star}{dt^{\star 2}} + b^\star\frac{dx^\star}{dt^\star} + k^\star x^\star = C_x(t), \tag{6.14}$$

where the force coefficient is defined as earlier: $C_x(t) = 2F_x(t)/(\rho V_\infty^2 DL)$.

At the end of each time step after calculation of the force acting on the cylinder, the equation of motion for an undamped cylinder is solved based on (6.14). Here, the right hand side of (6.14) is determined by integrating the source term in the x-direction momentum equation over the whole volume. Equation (6.14) is then split into a system of two 1st order ODEs:

$$\frac{dx^\star}{dt^\star} = v^\star, \tag{6.15}$$

$$m^\star\frac{dv^\star}{dt^\star} + b^\star v^\star + k^\star x^\star = C_x(t). \tag{6.16}$$

Solely, the system of equations are solved using a first order Euler backward scheme

$$x^{n+1} = x^n + \Delta t v^n, \tag{6.17}$$

$$v^{n+1} = v^n + \frac{\Delta t}{m^\star}\left[C_x(t) - b^\star v^n - k^\star v^n\right]. \tag{6.18}$$

CHAPTER 7

Post-processing Tools

This chapter describes briefly the kernel of the toolboxes used in the post-processing procedure of the conducted simulations, which are the two decomposition techniques, POD and DMD, for obtaining approximated descriptions of multidimensional systems in a statistical manner.

7.1 Proper Orthogonal Decomposition (POD)

The vortex shedding characteristics and the flow pattern behind moving objects such as cylinders and cantilevered beams are substantially altered during fluid-structure interaction which leads to the demand of a comprehensive understanding of the non-linear behaviour in the flow field. For this reason, a statistical approach based on Proper Orthogonal Decomposition (POD), as presented by Berkooz et al. [107] is used in this thesis to extract the coherent structures, referred as dynamics with temporal life cycle which captures relevant spatial scales.

The POD procedure extracts a basis for a modal decomposition of a given ensemble of data, e.g. velocity, pressure, vorticity etc. The data ensemble, which may contain scalar- or vector-valued functions, can be obtained experimentally or numerically and (for simplicity) it

is introduced in the context of the scalar velocity field v_j. Given this ensemble data $v(x,t)$, the POD is applied by seeking a base of spatial eigenfunctions $\Psi(x)$ such as

$$v(x,t) = a_0\Psi_0(x) + \sum_{n=1}^{\infty} a_n(t)\Psi_n(x), \tag{7.1}$$

where the first and second term of (7.1), represents the mean field (mode 0) and the dynamics of the flow field (the subsequent modes), respectively, and $a_n(t)$ are the time coefficients. Especially, $\Psi(x)$ is sought such that the quantity

$$\frac{\langle |(v,\Psi)|^2 \rangle}{\|\Psi\|^2}, \tag{7.2}$$

is maximized. Here, $< \cdot >$ denotes an ensemble average, $(\centerdot,\centerdot)$ an appropriate inner product and $\| \centerdot \|$ a norm for the space $\mathcal{L}^2(\Omega_x)$ of square integrable functions, where Ω_x is the physical domain considered. The physical meaning of (7.2) is that the procedure seeks to decompose the ensemble of realizations of the function $v(x,t)$ onto a base that would maximize the variance content of the N-first modes for any integer N, as reported by Berkooz et al. [107]. Nevertheless, the problem formulation of (7.2) can be recast as the solution of the Euler-Lagrange integral equation by applying the variational calculus according to

$$\int_{\Omega_x} \langle v(x)\ v(x') \rangle \Psi(x')\ dx' = \lambda\Psi(x), \tag{7.3}$$

which represents an eigenvalue problem whose kernel is the cross-correlation tensor, defined as $R(x,x') = \langle v(x)\ v(x') \rangle$. To each eigenvalue λ_n corresponds an eigenfunction Ψ_n or POD-mode. The eigenvalues are ordered in decreasing order ($\lambda_n > \lambda_{n+1}$) and the modes are normalized so that $(\Psi_n, \Psi_n) = 1$. Furthermore, with reference to (7.2), the POD modes are optimal in the sense of capturing, on average, the greatest possible fraction of total kinetic energy for a projection onto a given number of modes, as reported by Smith et al. [108]

In practice the field variable $v(x,t)$ is collected on a discrete grid and therefore is not a continuous function of time. Instead the field

realizations consist of a finite number N, where each of these has a value $v^k(x_m, t_k)$ in each of the M grid points as:

$$v^k = \begin{Bmatrix} a_1^k \\ a_2^k \\ \vdots \\ a_M^k \end{Bmatrix}, \quad k = 1, ..., N. \tag{7.4}$$

This leads to solving an eigenvalue problem with matrix dimensions $(M \times M)$, which is not computationally a feasible procedure. Instead, the discretization of the eigenvalue problem has been performed by using the so-called *Method of Snapshots* presented by Sirovich [109], which transforms (7.3) into an $(N \times N)$ eigenvalue problem, where N is the number of samples (snapshots). With this method the discretized eigenvalue problem in matrix form is formulated as:

$$\begin{bmatrix} b^{(1,1)} & \dots & b^{(1,N)} \\ b^{(2,1)} & \dots & b^{(2,N)} \\ \vdots & \ddots & \vdots \\ b^{(N,1)} & \dots & b^{(N,N)} \end{bmatrix} \begin{bmatrix} c^{(1)} \\ c^{(2)} \\ \vdots \\ c^{(N)} \end{bmatrix} = \lambda \begin{bmatrix} c^{(1)} \\ c^{(2)} \\ \vdots \\ c^{(N)} \end{bmatrix}, \tag{7.5}$$

where

$$b^{(j,k)} = \int_{\Omega_x} v^{(j)}(x)\, v^{(k)}(x)\, dx, \qquad c^{(k)} = \int_{\Omega} v^{(k)}(x')\, \Psi^{(}x')\, dx'. \tag{7.6}$$

Equation (7.5) is an $N \times N$ eigenvalue problem where the corresponding solution consists of N eigenvectors c_n with N eigenvalues λ_n. This allows the eigenfunctions, i.e. the POD modes to be reconstructed from the coefficients $c_n^{(k)}$ via

$$\Psi_n(x) = \frac{1}{\lambda_n N} \sum_{k=0}^{N} c_n^{(k)} v^{(k)}(x), \tag{7.7}$$

which reveals the eigenfunctions as linear combinations of the snapshots. The time coefficients may be computed by projecting the POD modes

onto the velocity field [107, 108], which for the n-th mode and k-th sample reads:

$$a_n^k = \sum_{m=1}^{M} \Psi_n(x_m)\, v_m^k. \tag{7.8}$$

In the exploratory work of this thesis the above mentioned approach was used in order to evaluate the POD modes [106]. In PAPER3 however, the POD modes have been extracted using a singular value decomposition. Basically, a correlation matrix of the field variables is singular value decomposed such that instead of solving a large ($M \times M$) eigenvalue problem one may instead solve a (typically) smaller one ($N \times N$) (as is the case in Sirovich method) and then calculate the desired POD modes. The reader is referred to PAPER3 for the details.

7.2 Dynamic Mode Decomposition (DMD)

Dynamic Mode Decomposition is a recently developed data-based method for extracting dynamic information from a data set sampled at a fixed temporal/spatial interval [110, 111]. The method to extract the dynamical characteristics, is applicable to both experimental and numerical flow field data and no explicit information about the underlying system matrix ($\mathbf{A}$) is needed.

Generally, a temporal snapshot sequence of N data fields consisting of a set of column vectors $\{v_i\}_{i=1}^{N}$, $v_k \equiv v(t_k)$, can be presented as

$$\mathbf{V}^N = \left[v_1, v_2, v_3, ..., v_N\right], \tag{7.9}$$

where an ordered sequence of data is expected to take place, separated by a constant sampling time $\triangle t$. As a first step, it is assumed that the flow field, v_k, can be written as a linear combination of the subsequent flow field v_{k+1}, by using a linear operator $\mathbf{A}$

$$v_{k+1} = \mathbf{A} v_k, \tag{7.10}$$

for $k = 1, 2, ..., N-1$. This assumption gives a linear tangent approximation since the original data set stems from the non-linear Navier-Stokes equations. Moreover, the procedure allows for computing approximate

eigenvalues and eigenvectors simply by projecting the high-dimensional matrix $\mathbf{A}$ onto a *Krylov* subspace assuming the linear mapping is constant.

It can be shown that as the number of snapshots increases (as the data sequence given by $\mathbf{V}^N$ captures the underlying physical process), the flow field given by (7.10) is assumed to approach a linear dependency. When this limit is reached, i.e. beyond a critical number of snapshots, the vector v_N can be expressed as a linear combination of the previous $N-1$ vectors v_i,

$$v_N = \sum_{i=1}^{N-1} v_i c_i + r, \tag{7.11}$$

where r is the residual and $\{c_i\}_{i=1}^{N-1} = \{c_1, c_2, ..., c_{N-1}\}$ are the weights. Following [112], the weights c_i are obtained via least squares calculation so as to minimize the residual, since equation (7.11) is an overdetermined system. This yields

$$\mathbf{A}\mathbf{V}^{N-1} = \mathbf{V}^{N-1}\mathbf{W} + \mathbf{r}\mathbf{e}_{N-1}^T, \tag{7.12}$$

where the matrix $\mathbf{W}$ is of companion type and given by

$$\mathbf{W} = \begin{bmatrix} 0 & 0 & \dots & 0 & c_0 \\ 1 & 0 & & 0 & c_1 \\ 0 & 1 & & 0 & c_2 \\ \vdots & & \ddots & & \vdots \\ 0 & 0 & \dots & 1 & c_{N-1} \end{bmatrix}. \tag{7.13}$$

The $\mathbf{W}$ matrix typically approximates a low-dimensional system matrix representation of the full system matrix $\mathbf{A}$, with a solution that approximates some of the eigenvalues (λ_j) of $\mathbf{A}$. Thus, the problem becomes one of finding the eigenpairs (λ, x) for the matrix $\mathbf{W}$,

$$\mathbf{W}\mathbf{x} = \lambda\mathbf{x}, \tag{7.14}$$

where the eigenvectors, $\mathbf{x}$, provide a linear combination of basis coefficients in order to extract the corresponding *dynamic modes*

$$\Psi_j = \mathbf{V}^{N-1}\mathbf{x}_j. \tag{7.15}$$

The associated eigenvalues (λ_j) provides the growth rate, $\sigma_j = \Re\{ln\,(\lambda_j)\}$ $/\triangle t$, and the frequency, $f_j = \Im\{ln\,(\lambda_j)\}/2\pi\triangle t$, of the corresponding eigenmode Ψ_j.

The **W**-matrix method might cause an ill-coonditioned algorithm when extracting the dominant dynamic modes [110]. An alternative to the companion matrix yielding a more robust implementation is the so-called 'full matrix' approach, $\widetilde{\mathbf{W}}$, which is related to **W** via a similarity transformation by using a singular value decomposition of the extracted flow field data [110]. Both of these methods have been used in this thesis, where the DMD formulations based on $\widetilde{\mathbf{W}}$ can be seen in PAPER3.

CHAPTER 8

Unpublished Work

The experimental study of an elastically mounted circular cylinder was performed in collaboration with Dr. S.M. Hosseini, who also designed the cylinder and conducted image processing of the gathered data.

Experimental Study of VIV of a Circular Cylinder

The present experiments were performed in a confined water-channel made of plexiglass, at Lund University. The working section had a cross-section area of 10 cm $\times$ 10 cm and a length of 30 cm. The free-stream velocity V_∞ was varied in between 0.042 m/s and 0.28 m/s in order to capture the expected high-amplitude of oscillations from numerical simulations. The cylinder was 9.16 cm long and had a diameter D of 1 cm giving an aspect ratio of 9.16. Moreover, the supporting plates at which the ball bearings were placed had a thickness of 0.34 cm each. The diameter d of the ball bearings were varied between 0.3 and 0.4 cm depending on the relative resistance to the cross-section. The Reynolds number based on the free-stream velocity V_∞, the cylinder diameter D

and a kinematic viscosity ν at room temperature (24 Celsius degrees) of 1.004 x 10^{-6} m^2/s was, analogous to the free-stream velocity, varied between 415 and 2759.

Within numerical simulations the response dynamics is presented in the plane of $\{A^\star, V^\star\}$ and $\{(f^\star/f_N^\star), V^\star\}$. For this reason, a corresponding set of structural- and flow parameters has to be chosen in the experiments in order to be able to match an equivalent flow regime as for numerical simulations. Nevertheless, the matching of equivalent flow conditions (between numerical simulations and experiments) requires suitable pump equipment and correct stiffness, since $f_N = \frac{1}{2\pi}\sqrt{\frac{k}{m}}$ and $V^\star = V/(f_N D)$. For this set of experiments a cylinder made of plexiglass with a density of $\rho_{plexyglas} = 1190$ kg/m^3 was used. Moreover, the rigid cylinder was assembled symmetrically in the test-section with four extension-springs mounted on each side (up and down), where each spring had a stiffness of k = 6 N/m. Further, before the experiments could start a pre-calibration was conducted in order to evaluate the actually spring stiffness experienced of the complete set of cylinder-spring system in the transverse direction to the free-stream flow. From the calibration data the (averaged) stiffness of the cylinder-spring system is evaluated to $k_{stiffness}$ = 3.22 N/m. A schematic diagram of the experimental arrangement and the rigid cylinder in the test-section, which is allowed to move in two-degrees of freedom is shown in Figure 8.1 and 8.2, respectively.

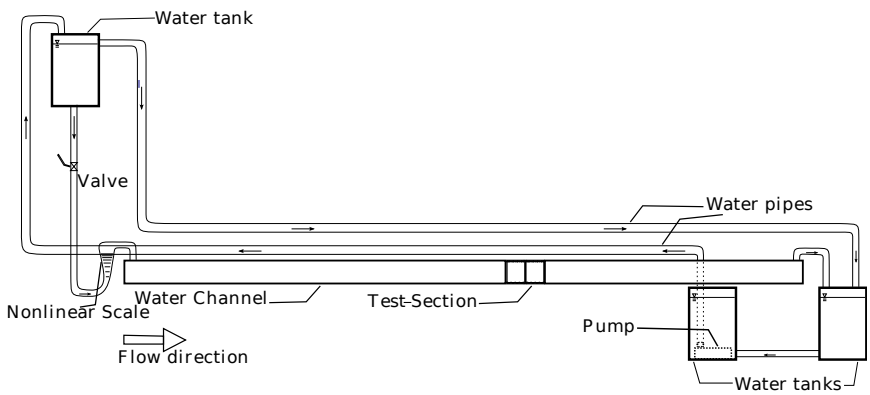

Figure 8.1: A schematics of the experimental arrangement.

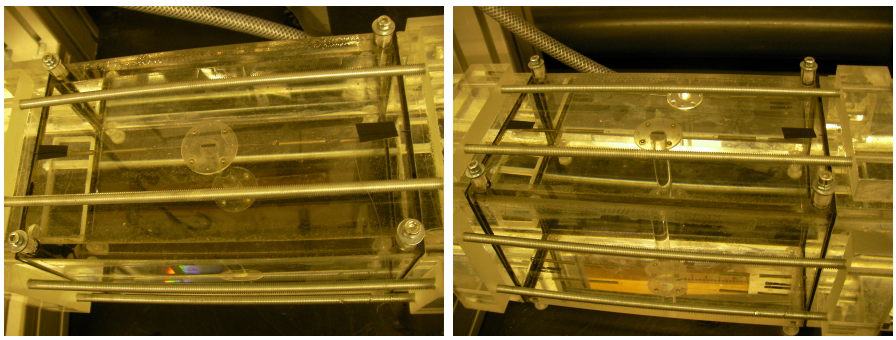

Figure 8.2: Pictures of the cylinder assembling in the test-section.

Image Processing

The amplitude and frequency motion of the cylinder, and, the lift and drag forces was measured by using a high-speed Phantom $V7.1$ camera composed of 256 $\times$ 256 pixels and 200 fps frame rates. In total, 6000 frames were captured in each measurement and the time difference between each two frame was 0.005 sec. Each image has a size of 30 $\times$ 30 mm^2, which yields a resolution of 0.12 mm/pixel.

For post-processing of the data, a 'movement target' consisting of a black tape of rectangular shape was assembled on the center of the cylinder's cross sections with the size of 1.2 $\times$ 7.8 mm, which is 100 times smaller than the displacement of the cylinder. Figure 8.3 (a) and 8.3 (b) show the moving target and a sample of one particular image, respectively.

Further, the collected data was evaluated by utilizing an image-processing program which detects the instantaneous motion of the moving target, i.e. the cylinder. This allows to calculate the amplitude of the motion by positioning the center of the rectangular target in each frame and in turn determine the displacement of the target between each two continual frames. The details of the image-processing can be described briefly (chronologically) as follows:

1. A Gaussian filter is applied to each image.

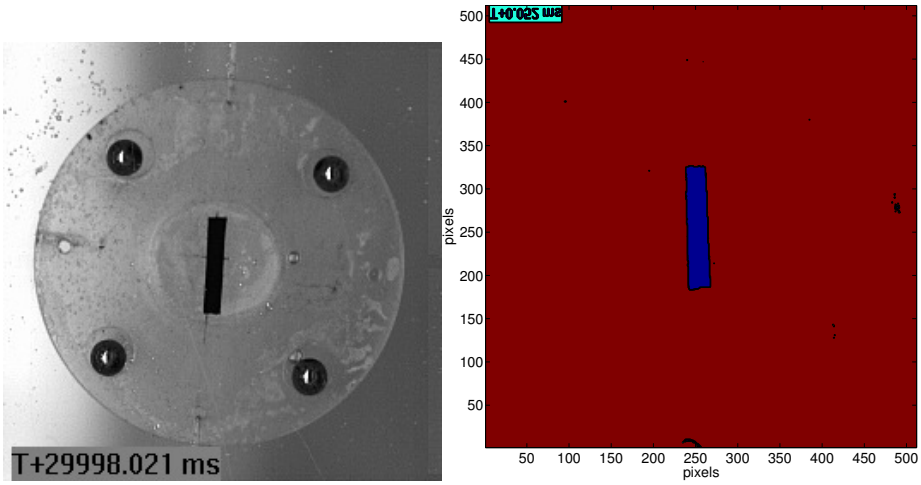

(a) A sample image. **(b)** Movement target.

Figure 8.3: Image processing and detection procedure.

2. A threshold value is evaluated based on the PDF distribution of each pixel value in order to convert all frames to binaries.
3. The binary frames are used to detect each pixel at the boundary of the target.
4. A straight line is fitted to each side of the target by using geometrical (x, y) information of the position of each pixel at the boundary.
5. A double PDF method is applied to calculate the slope of each fitting line.
6. The final shape of the target is determined by estimating the area of the four fitting lines.
7. Finally, the position of the target, and hence the cylinder, is determined by evaluating the center of the target based on the previously calculated area.

Following this procedure, the velocity (v) and the acceleration (a) of the oscillating cylinder can be evaluated by evaluating the spatial $(\triangle x)$ and

temporal ($\triangle t$) distance between two frames according to:

$$v = \frac{\triangle x_i}{\triangle t_i}, \qquad a = \frac{v_{i+1} - v_i}{\triangle t_i}, \tag{8.1}$$

where i is the number of frame. The accuracy of the image-processing was estimated by evaluating the cross section of each rectangular target and compare with the calibration image. The total number of pixels in each target is 650 pixels and the uncertainty was estimated to ± 6 pixels, which gives an error of almost one percentage. Based on this, the maximum frequency of the cylinder motion was estimated to 10 Hz, which yields that at least 20 data points were collected in each cycle (between upper and lower turning points) of oscillation since the frame rate was 200 Hz.

Preliminary Results

The experimental results of the cylinder, allowed to move in-line and transverse to the fluid flow, is depicted in Figure 8.4. The presented results are shown only for the transversal motion though. Here, it can be observed that the amplitude response is represented by the initial and the lower branches for low and high reduced velocities, respectively. Further, the characteristics of the amplitude of motion shows that perceptible high-amplitude of oscillations, characterized by the synchronization-range, occurs for reduced velocities in the range, $V^\star \approx 3 - 6$. This behaviour seems to be a reduced version of the data presented by Khalak and Williamson [3] and Cesur [5], at which the synchronization region appears for $V^\star \approx 3 - 10$ and $V^\star \approx 4 - 9$, respectively. In addition, the maximum amplitude of oscillations seems to be reduced with a factor of about 1.36 compared with the numerical simulations of Cesur [5], which where performed for similar flow and set-up conditions.

The frequency response of the cylinder motion shows that, even though not as distinct, that the cylinder-spring system is composed of a the three-fold dynamic state, i.e. the shedding frequency for a stationary cylinder, the natural frequency in still-water and the in vacuo natural frequency.

The explanation for the discrepancy between the experiments and found results (as those mentioned above) may be related to a series of

sources. Among these, the human factor is one of them e.g. in the assembling process, in the camera monitoring and in particular in the process of flow regulation for desired level. Besides these influences, it was observed during the experiments that the cylinder was intermittently inhibited in its motion, changing between a rapid and slow, but incoherent motion for a given flow rate. It is not yet known whether if this behaviour is caused by uncontrolled friction in the test-section or if it is actually the free-stream turbulence that alters the cylinder response dynamics since, with reference to Khalak and Williamson [3] and other related co-works, no free-stream turbulence has been reported in their experimental studies.

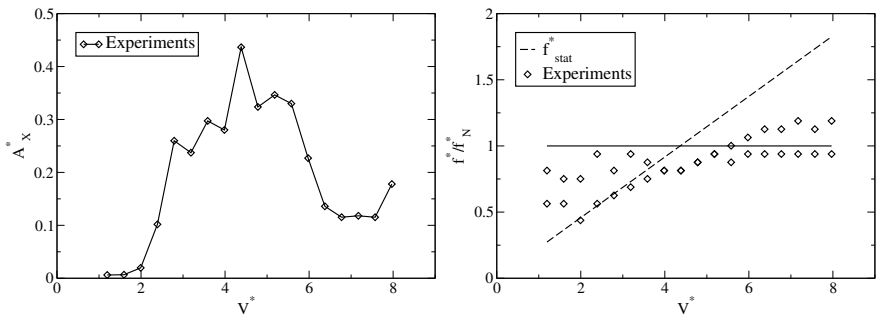

Figure 8.4: Amplitude and frequency response of the transversal cylinder motion from experiments for $m^{\star}$=1.35.

CHAPTER 9

Concluding Remarks

This chapter presents the overall achieved conclusions in this thesis work, which are based on the results of four manuscripts. For a better understanding, the reader is primarily referred to these manuscripts.

Large eddy simulations of fluid-structure interaction problems are carried out in this thesis work. The main effort has been placed on clarifying in which way and how flow structures in the near-wake of certain bluff bodies interact with the corresponding objects.

The results of three-dimensional flow around an elastically mounted circular cylinder show that a strong shedding mechanism dominates completely the flow in the synchronization region. When the cylinder is at a state just prior to the initial branch the natural frequency clearly dominates the cylinder motion unlike its corresponding wake structure contributing with relatively weak influence. For the posterior part of the lower branch, although the cylinder-wake dynamics have similarities with 'prior-to-the initial branch', the flow-cylinder dynamics was rather complicated and the inherent frequency content was much more broadband. In summary, it was suggested that vortex-pairing of a low-frequency mode and vortex shedding was the underlying mechanism of the flow-(single) cylinder dynamics.

Non-staggered (and similarly for staggered) multiple cylinders at 'prior-to-the initial branch' showed that upstream cylinders oscillate in-phase. The symmetry of the dominating wake structure was, however, the same as in the synchronization region, where the upstream and downstream cylinder pairs oscillated (almost) 180° out-of phase. A similar observation was found for a very resilient mode in the posterior part of the lower branch for multiple cylinders placed in a non-staggered arrangement. Two opposing mechanisms were suggested, one competing for the (upstream) cylinders to oscillate in phase, and the other one being the ordinary shedding for an oscillation (roughly) 180° out-of phase.

A low-frequency mode (representative for a specific decomposed wake structure) was also detected in the simulations of both stiff and flexible cantilever beam. It was observed to be formed around the separation region behind the beam with rather large structures. It was enthralling to realize (by verification) that the interaction of this low-frequency mode with the shedding mode induced new modes, which in turn gave rise, through interference effects, to a beat frequency in the force and displacement. As a result, an increase in the concentration of near-wake structures around the flexible beam could be observed (via projection of modes) at certain instants in the temporal domain which was seen as increased transversal and streamwise forces attained at the beam.

As a close-up, a direct one-to-one tracing of the mutual beam-wake dynamics was conducted to outline the difference in the dynamics between a stiff and a cantilever beam. This was done for one loading cycle, consisting of moderate and intensive forcing, by investigating the characteristics of the unsteady flow structures in the wake in conjunction with the response of the beams. The difference(s) in the high forcing situation between the two beams was coupled to the change in the entrainment effect associated with the downwash flow, which for the flexible beam, is not able to disturb the von-Kármán vortices shed from the side-walls of the beam as intense as for the stiff beam case. Hence, the enhancement of the strength of the von-Kármán vortices in conjunction with a decrease of the base pressure (due to a less downwash) behind the beam leads to an increase of the total forces in the different directions.

CHAPTER 10

Summary of Publications

PAPER I

A. Feymark, **A. Cesur**, N. Alin, C. Fureby, J. Revstedt, R. Bensow. "Fluid-Structure Interaction using Parallel Open Source Software with Application in Hydroelasticity". *Submitted to Journal of Computational Physics, 2013.*

In this paper a numerical methodology based on Implicit Large Eddy Simulation capable of providing high fidelity predictions of Fluid-Structure Interaction with application in hydroelasticity is proposed. Furthermore, a fully parallel and strongly coupled solution algorithm is utilized in order to avoid numerical instability phenomena. One major reason to instability is the added mass effect, typically arising when the densities of fluid and solid are comparable as in hydroelasticity. The use of Large Eddy Simulation is motivated by the transient nature of, for instance, propeller induced vibrations and noise. The implementation relies on open source toolkits only, with OpenFOAM as flow solver and OOFEM as the structural solver. The numerical accuracy, convergence, and efficiency, of the FSI methodology, are benchmarked while predicting the deformations of

a flexible cantilever beam in a cross-flow. Furthermore, a validation procedure is performed, comparing predictions with the experimental data of a deforming hydrofoil. The whole methodology is found to be robust and stable.

The author carried out the numerical simulations and was one of the two main responsible writers of the paper. Further, the author contributed in developing a structural solver required for the FSI simulations of a deformable cantilever.

PAPER II

A. Cesur, A. Feymark, J. Revstedt. "A Large Eddy Simulation Based Fluid-Structure Interaction Study of a Stiff and a Flexible Cantilever Beam". *Submitted to Journal of Physics of Fluids, 2013.*

The force loading on a cantilever beam is characterized by periodically occurring low and high force fluctuations, here denoted moderate and intensive states, respectively. In this work detailed qualitative studies of the wake flow for each of these responses are performed, both stiff and flexible (i.e. elastically deforming) cantilevers. The flow is simulated using an implicit large eddy simulation (ILES) approach in OpenFOAM and the structural deformation of the beam is found from a non-linear finite element approach using OOFEM. The motion of the fluid mesh due to the structural deformation is handled by an ALE method. The results reveal an intricate interaction between the vortices causing these two distinctly different states and that the deformation of the cantilever further ads to the complexity of the wake structures.

The author carried out the transient part of the numerical simulations, participated in the post-processing of the results and wrote a major part of the paper.

PAPER III

A. Cesur, C. Carlsson, A. Feymark, L. Fuchs, J. Revstedt. "Analysis of the Wake Dynamics of Stiff and Flexible Cantilever Beams using POD and DMD". *Submitted to Journal of Computers & Fluids, 2013.*

The wake flow behind a cantilever beam of quadratic cross-section at a Reynolds number of 50000 is investigated using detailed simulation. Two cases are considered, the first one using a stiff beam and the second one with a beam allowing for flexible deformation of the beam due to the hydrodynamic forces. The flow is simulated using an implicit large eddy simulation (ILES) approach in OpenFOAM and the structural deformation of the beam is found from a non-linear finite element approach using OOFEM. The motion of the fluid mesh due to the structural deformation is handled by an ALE method. The wake structures are investigated using proper orthogonal decomposition (POD) and dynamic mode decomposition (DMD) of the flow field. The results show that apart from the wake structures originating from the vortex shedding there is also a low frequency mode, which is an oscillatory motion in the stream-wise direction present.

The author carried out the transient part of the numerical simulations, participated in the post-processing of the results and wrote a major part of the paper.

PAPER IV

A. Cesur, C. Carlsson, L. Fuchs, J. Revstedt. "Modal Analysis for Oscillating Cylinder Arrays at Low Reynolds number". *Submitted to Journal of Fluids and Structures, 2013.*

A numerical study of three-dimensional flow around an elastically mounted single cylinder have been investigated using implicit Large Eddy Simulations (ILES). The simulations are conducted for laminar flow at the Reynolds number of 400, based on the bulk velocity and the cylinder diameter. The core of the investigation was focused to outline the corre-

lation between cylinder response dynamics and its associated wake structures when exposed to VIV using Fast Fourier Transform (FFT) analysis together with the flow decomposition technique called, Dynamic Mode Decomposition (DMD). This was done for three different reduced velocities, $V^{\star}$=2.5, 6.0 and 12.0, corresponding to specific flow and cylinder dynamics just before the initial branch, at the lower branch lock-in and posterior part of the lower branch, respectively. The findings for a single cylinder was carried over to a group of four circular cylinders, also elastically mounted, in a quadratic and staggered arrangements. The strength of Dynamic Mode Decomposition, by reducing the large number of degrees of freedom to only a limited set of modes, is seen as advantageous for extracting dynamics with specific frequencies when compared to e.g. Proper Orthogonal Decomposition (POD).

Bibliography

[1] A. Roshko. On the development of turbulent wakes from vortex streets. Technical report, Technical Note 2913, 1953.

[2] C. Norberg. An experimental investigation of the flow around a circular cylinder: influence of aspect ratio. *Journal of Fluid Mechanics*, 258:287–316, 1992.

[3] A. Khalak and C.H.K. Williamson. Fluid forces and dynamics of a hydroelastic structure with very low mass and damping. *Journal of Fluids and Structures*, 11:973–982, 1997.

[4] C.C. Feng. The measurement of vortex-induced effects in flow past a stationary and oscillating circular and d-section cylinders. Master's thesis, University of British Columbia, Vancouver, B.C., Canada, 1968.

[5] A. Cesur. A numerical study of fluid-structure interaction of non-deformable cylinders, thesis for the degree of licentiate in engineering, 2011.

[6] F. Flemming and C.H.K. Williamson. Vortex-induced vibrations of a pivoted cylinder. *Journal of Fluid Mechanics*, 522:215–252, 2005.

[7] C.P. Pesce and A.L.C. Fujarra. Vortex-induced vibrations and jump phenomenon: Experiments with a clamped flexible cylinder in water. *International Journal of Offshore and Polar Engineering*, 10(1), 2000.

[8] A. Khalak and C.H.K. Williamson. Investigation of the relative effects of mass and damping in vortex-induced vibration of a circular cylinder. *Journal of Wind Engineering and Industrial Aerodynamics*, 60 - 71:341 – 350, 1997.

[9] J. Revstedt. Interactions between an incompressible flow and elastic cantilevers of circular cross-section. *Conference on Modelling Fluid Flow (CMFF'12), The 15th International Conference on Fluid Flow Technologies, Budapest, Hungary, September 4-7, 2012*, 2012.

[10] A.L.C. Fujarra, C.P. Pesce, F. Flemming, and C.H.K. Williamson. Vortex-induced vibration of a flexible cantilever. *Journal of Fluids and Structures*, 15(3 - 4):651 – 658, 2001.

[11] C. Farhat, K. G. van der Zee, and P. Geuzaine. Provably second-order time-accurate loosely-coupled solution algorithms for transient nonlinear computational aeroelasticity. *Computer Methods in Applied Mechanics and Engineering*, 195(1718):1973 – 2001, 2006.

[12] David N. Ku. Blood flow in arteries. *Annual Review of Fluid Mechanics*, 29(1):399–434, 1997.

[13] R.L. Campbell and E.G. Paterson. Fluid-structure interaction analysis of flexible turbomachinery. *Journal of Fluids and Structures*, 27:1376–1391, 2011.

[14] OOFEM. Free object oriented finite element code @ONLINE, January 2012.

[15] B. Patzák. Design of object oriented finite element code. *Advances in Engineering Software*, 32:759–767, 2001.

[16] O. Reynolds. An experimental investigation of the circumstances which determine whether the motion of water shall be direct or

sinuous, and the law of resistance in parallel channels. *Philosophical Transactions of the Royal Society of London*, 174:935–982, 1883.

[17] V. Strouhal. Ueber eine besondere art der tonerregung. *Ann. Phys. und Chemie*, 5(10):216–251, 1878.

[18] A. Roshko. On the drag and shedding frequency of two-dimensional bluff bodies. Technical report, Technical Note 3169, 1954.

[19] G. Kirchhoff. Zur theorie freier flussigkeitsstrahlen. *Journal of Mathematics*, 70:289–298, 1869.

[20] T. von Karman. Collected works (4 volumes), 1975.

[21] P.W. Bearman. Vortex shedding from oscillating bluff bodies. *Annual Review of Fluid Mechanics*, 16:195–222, 1984.

[22] J.H. Gerrard. The mechanics of the formation region of vortices behind bluff bodies. *Journal of Fluid Mechanics*, 25:401–413, 1966.

[23] A. Fage and F.C. Johansen. The flow of air behind an inclined flat plate of finite span. *British ARC R and M*, 3120, 1927.

[24] F.H. Abernathy and R.E. Kronauer. The formation of vortex streets. *Journal of Fluid Mechanics*, 13:1–20, 1962.

[25] P.W. Bearman. Investigation of the flow behind a two-dimensional model with a blunt trailing edge and fitted with splitter plates. *Journal of Fluid Mechanics*, 21:241–255, 1965.

[26] P.W. Bearman. The effect of base bleed on the flow behind a two-dimensional model with a blunt trailing edge. *Aeronautical Quarterly*, 18:207–224, 1967.

[27] V.D. Narasimhamurthy and H.I. Andersson. Numerical simulation of the turbulent wake behind a normal flat plate. *International Journal of Heat and Fluid Flow*, 30:1037–1043, 2009.

[28] J. Dusek, P. Fraunie, and P. Le Gal. Local analysis of the onset of instability in shear flows. *Physics of Fluids*, 6:172, 1994.

[29] C.H.K. Williamson. The existence of two stages in the transition to three-dimensionality of a cylinder wake. *Physics of Fluids*, 31:3165, 1998.

[30] G.D. Miller and C.H.K. Williamson. Control of three-dimensional phase dynamics in a cylinder wake. *Experiments in Fluids*, 18:26–35, 1994.

[31] K. Ryan, M.C. Thompson, and K. Hourigan. Three-dimensional transition in the wake of elongated bluff bodies. *Journal of Fluid Mechanics*, 538:1–29, 2005.

[32] G. Schewe. On the force fluctuations acting on a circular cylinder in crossflow from subcritical to transcritical reynolds numbers. *Journal of Fluid Mechanics*, 133:265–285, 1983.

[33] A. Khalak and C.H.K. Williamson. Motions, forces and mode transitions in vortex-induced vibrations at low mass-damping. *Journal of Fluids and Structures*, 13:813–851, 1999.

[34] B.J. Vickery and R.D. Watkins. Flow-induced vibrations of cylindrical structures. In R. Silvester, editor, *Hydraulics and Fluid Mechanics: Proceedings of the First Australian Conference on Hydraulics and Fluid Mechanics*, pages 6–13. New York: Pergamon Press, 1964.

[35] S. Scruton. On the wind-excited oscillations of towers, stacks and masts. In R. Silvester, editor, *Proceedings of the Symposium on Wind Effects on Buildings and Structures*, pages 798–836. London: Her Majesty's Stationery Office, 1965.

[36] R.A. Skop and O.M. Griffin. An heuristic model for determining flow-induced vibrations of offshore structures. *5th Offshore Technology Conference*, 1973.

[37] C.H.K. Williamson and R. Govardhan. Vortex-induced vibrations. *Annual Review of Fluid Mechanic*, 36:413–455, 2004.

[38] R.A. Skop and S. Balasubramanian. A new twist on an old model for vortex-excited vibrations. *Journal of Fluids and Structures*, 11:395–412, 1997.

[39] T. Sarpkaya. Vortex-induced oscillations. *Journal of Applied Mechanics*, 46:241–258, 1979.

[40] M.M. Zdravkovich. On origins of hysteretic responses of a circular cylinder induced by vortex shedding. *Zeitschrift fur Flugwissenschaften Weltraumforschung*, 14:47–58, 1990.

[41] K. Vikestad, J.K. Vandiver, and C.M. Larsen. Added mass and oscillation frequency for a circular cylinder subjected to vortex-induced vibrations and external disturbance. *Journal of Fluids and Structures*, 14:1071–1088, 2000.

[42] I. Borazjani and F. Sotiropoulos. Vortex-induced vibrations of two cylinders in tandem arrangement in the proximity-wake interference region. *Journal of Fluid Mechanics*, 621:321–364, 2009.

[43] T. Sarpkaya. Hydrodynamic damping, flow-induced oscillations, and biharmonic response. *ASCE Journal of Offshore Mechanics and Arctic Engineering*, 117:232–238, 1995.

[44] N. Jauvtis and C.H.K. Williamson. Vortex-induced vibration of a cylinder with two degrees of freedom. *Journal of Fluids and Structures*, 17:1035–1042, 2003a.

[45] N. Jauvtis and C.H.K. Williamson. A high-amplitude 2t mode of vortex formation, and the effects of non-harmonic forcing in vortex-induced vibration. *European Journal of Mechanics - B/Fluids*, 2003b. In press.

[46] N. Jauvtis and C.H.K. Williamson. The effects of two degrees of freedom on vortex-induced vibration. *Journal of Fluid Mechanics*, 2003c. Submitted.

[47] C.H.K. Williamson and A. Roshko. Vortex formation in the wake of an oscillating cylinder. *Journal of Fluids and Structures*, 2:355–381, 1988.

[48] R. Govardhan and C.H.K. Williamson. Modes of vortex formation and frequency response of a freely vibrating cylinder. *Journal of Fluid Mechanics*, 420:85–130, 2000.

[49] A.H. Techet, F.S. Hover, and M.S. Triantafyllou. Vortical patterns behind a tapered cylinder oscillating transversely to a uniform flow. *Journal of Fluid Mechanics*, 363:79 – 96, 1998.

[50] P. Anagnostopoulos and P.W. Bearman. Response characteristics of a vortex-excited cylinder at low reynolds numbers. *Journal of Fluids and Structures*, 6:39 – 50, 1992.

[51] B.J. Vickery and R.D. Watkins. Two and three-dimensional simulations of vortex-induced vibration of a circular cylinder. *Proceedings of the 3rd International Offshore polar Engineering Conference*, 3:715–20, 1993.

[52] D.J. Newman and G.E. Karniadakis. Direct numerical simulations of flow over a flexible cable. *Proceedings of the 6th International Conference of Flow-Induced Vibrations*, pages 193 – 203, 1992. ed. P.W. Bearman, Rotterdam, Netherlands:Balkena.

[53] D. Shiels, A. Leonard, and A. Roshko. Flow-induced vibration of a circular cylinder at limiting structural parameters. *Journal of Fluids and Structures*, 15:3–21, 2001.

[54] J. Carberry and J. Sheridan. Forces and wake modes of an oscillating cylinder. *Journal of Fluids and Structures*, 15:523–532, 2001.

[55] A. Leonard and A. Roshko. Aspects of flow-induced vibration. *Journal of Fluids and Structures*, 15:415–425, 2001.

[56] J. Carberry, J. Sheridan, and D. Rockwell. Controlled oscillations of a cylinder: a new wake state. *Journal of Fluids and Structures*, 17:337–343, 2003.

[57] J. Carberry, R. Govardhan, J. Sheridan, D. Rockwell, and C.H.K Williamson. Wake states and response branches of forced and freely

oscillating cylinders. *European Journal of Mechanics - B/Fluids*, 23:89–97, 2004.

[58] T.L. Morse and C.H.K. Williamson. Fluid forcing, wake modes, and transitions for a cylinder undergoing controlled oscillations. *Journal of Fluids and Structures*, 25:697–712, 2009a.

[59] T.L. Morse and C.H.K. Williamson. Prediction of vortex-induced vibration response by employing controlled motion. *Journal of Fluid Mechanics*, 634:5–39, 2009b.

[60] T.L. Morse and C.H.K. Williamson. Employing controlled vibrations to predict fluid forces on a cylinder undergoing vortex-induced vibration. *Journal of Fluids and Structures*, 22:877–884, 2006.

[61] C.P. Pesce and A.L.C. Fujarra. Vortex-induced vibrations and jumping phenomenon: An experimental investigation with a clamped flexible cylinder in water. *International journal of Offshore and Polar Engineering*, 420:26 – 33, 2000.

[62] C.T. Yamamoto, J.R. Meneghini, F. Saltara, R.A. Fregonesi, and J.A. Ferrari Jr. Numerical simulations of vortex-induced vibration on flexible cylinders. *Journal of Fluids and Structures*, 19(4):467 – 489, 2004.

[63] H. Schlichting and K. Gersten. *Boundary-Layer Theory.* Springer-Verlag Berlin Heidelberg New York, 2000.

[64] J. O. Hirschfelder, C. F. Curtis, and R. B. Bird. *Molecular Theory of Gases and liquids.* Wiley, New York, 1954.

[65] I Demirdžić and M. Perić. Space conservation law in finite volume calculations of fluid flow. *Int J Numer Meth Fluids*, 8:1037 – 1050, 1998.

[66] K. Stein, T. Tezduyar, and R. Benney. Mesh moving techniques for fluid-structure interactions with large displacements. *Journal of Applied Mechanics*, pages 70–58, 2003.

[67] H. Jasak and Z. Tuković. Automatic mesh motion for the unstrtuctrued finite volume method. *Transactions of FAMENA*, 30(2):1–20, 2006.

[68] M.M. Rai and P. Moin. Direct simulations of turbulent flow using finite differences. *Journal of Computational Physics*, 96:15–53, 1991.

[69] L. Fuchs. Defect-corrections and higher numerical accuracy. *International Journal in Numerical Methods of Fluids*, 10:52–66, 1984. Proc. of the GAMM-workshop on 'Efficient Solvers for Elliptic Systems', Notes on numerical methods in Fluid mechanics.

[70] S.V. Patankar. Numerical predictions of three dimensional flows. In *Studies in Convection: Theory, Mesurement and Applications*, page 1. 1975.

[71] L. Fuchs and H.-S. Zhao. Solution of three dimensional viscous incompressible flow by a multi-grid method. *International Journal in Numerical Methods of Fluids*, 4:539–555, 1984.

[72] H. Jasak. Error analysis and estimation for the finite volume method with applications to flud flows. Imperial College, 1996. Doctoral thesis.

[73] J. Lambert. Computational methods in ordinary differential equations. Wiley, London, New York, 1973.

[74] OpenFOAM. The open source computational fluid dynamics(cfd) toolbox @ONLINE, January 2012.

[75] S. Pope. *Turbulent Flows*. Cambridge University Press, 2000.

[76] J.R. Hughes Thomas. *The Finite Element Method: Linear Static and Dynamic Finite Element Analysis*. Dover Publications, Mineola, NY, 2000.

[77] K. Bathe. *Finite Element Procedures*. Englewood Cliffs, New Jersey, 1996.

[78] S. Krenk. *Non-Linear Modelling and Analysis of Solids and Structures.* Cambridge University Press, Cambridge, UK New York, 2009.

[79] D.A. Dunavant. High degree efficient symmetrical gaussian quadrature rules for the triangle. *International Journal for Numerical Methods in Engineering*, 21:1129–1148, 1985.

[80] M. Gellert, R. Harbord, and M. Haroun. Moderate degree cubature formulas for 3-d tetrahedral finite-element approximations. *Communications in Numerical Methods in Engineering*, 7:487–495, 1991.

[81] K. Subbaraj and M.A. Dokainish. A survey of direct time-integration methods in computational structural dynamics - ii. implicit methods. *Computers and Structures*, 32:1387–1401, 1989.

[82] B. Fomberg. Generation of finite difference formulas on arbitrarily spaced grids. *Mathematics of Computation*, 51:699–706, 2006.

[83] M. Ristinmaa and C. Ljung. An introduction to stability analysis, 1998. Collected notes.

[84] C.A. Felippa, K.C. Park, and M.R. Ross. A classification of interface treatments for fsi. In *Fluid Structure Interaction II.* Springer-Verlag Berlin Heidelberg, 2010.

[85] M.C. Junger and D. Feit. *Sound, Structures and Their Interaction.* MIT Press, Cambridge Massachussets, 1972.

[86] W. Dettmer and D. Perić. A computational framework for fluid-structure interaction: Finite element formulation and applications. *Computer Methods in Applied Mechanics and Engineering*, 195:5754–5779, 1993.

[87] T.E. Tezduyar, S. Sathe, J. Pausewang, M. Schwaab, J. Christopher, and J. Crabtree. Interface projection techniques for fluid-structure interaction modelling with moving-mesh methods. *Computational Mechanics*, 53:39–49, 2008.

[88] C.A. Felippa, K.C. Park, and C. Farhat. Partitioned analysis of coupled mechanical systems. *Computer Methods in Applied Mechanics and Engineering*, 190:3247–3270, 2001.

[89] C. Michler, E.H. van Brummelen, S.J. Hulshoff, and R. de Borst. The relevance of conservation for stability and accuracy of numerical methods for fluid-structure interaction. *Computer Methods in Applied Mechanics and Engineering*, 192:4195–4215, 2003.

[90] S. Piperno, C. Farhat, and B. Larrouturou. Partitioned procedures for the transient solution of coupled aeroelastic problems-part ii: Energy transfer analysis and three-dimensional applications. *Computer Methods in Applied Mechanics and Engineering*, 190:3147–3170, 2001.

[91] R. Jaiman, P. Geubelle, E. Loth, and M.J. Xiangmin. Stable and accurate loosely-coupled scheme for unsteady fluid-structure interaction. *45th AIAA Aerospace Sciences Meeting and Exhibit*, 2007. Reno, Nevada.

[92] Proceedings of the Royal Society of Edinburgh. *On Bernouilli's Numerical Solution of Algebraic Equations*, volume 46, 1926.

[93] K. Bathe and H. Zhang. Finite element developments for general fluid flows with structural interactions. *International Journal for Numerical Methods in Engineering*, 60(1):213–232, 2004.

[94] M. Lesoinne and C. Farhat. Geometric conservation laws for flow problems with moving boundaries and deformable meshes, and their impact on aeroelastic computations. *Computer Methods in Applied Mechanics and Engineering*, 134(1-2):71–90, 1996.

[95] M. Breuer, G. De Nayer, M. Münsch, T. Gallinger, and R. Wüchner. Fluid-structure interaction using a partitioned semi-implicit predictor-corrector coupling scheme for the application of large-eddy simulation. *Journal of Fluids and Structures*, 2012.

[96] C.S. Peskin. Numerical analysis of blood flow in the heart. *Journal of Computational Physics*, 25:220–252, 1977.

[97] D. Goldstein, R. Handler, and L. Sirovich. Modelling a no-slip flow boundary with an external force field. *Journal of Computational Physics*, 105:354–366, 1993.

[98] J. Mohd-Yusof. Combined immersed-boundary/b-spline methods for simulations of flow in complex geometries. *Center for Turbulence Research, Annual Research Briefs*, pages 317–327, 1997.

[99] E.A. Fadlun, R. Verzicco, P. Orlandi, and J. Mohd-Yusof. Combined immersed-boundary finite-difference methods for three-dimensional complex flow simulations. *Journal of Computational Physics*, 161:35–60, 2000.

[100] D.L. Young, Y.J. Jan, and C.L. Chiu. A novel immersed boundary procedure for flow and heat simulations with moving boundary. *Computer and Fluids*, 38:1145–1159, 2009.

[101] Y. Kim and C.S. Peskin. 3-d parachute simulation by the immersed boundary method. *Computer and Fluids*, 38:1080–1090, 2009.

[102] J. Revstedt. A virtual boundary method with improved computational efficiency using a multi-grid method. *International Journal for Numerical Methods in Engineering*, 45(7):775–795, 2004.

[103] E.A. Fadlun, R. Verzicco, P. Orlandi, and J. Modh-Yusof. Combined immersed-boundary finite-difference methods for three-dimensional complex flow situations. *Journal of Computational Physics*, 161:35–60, 2000.

[104] J. Revstedt and L. Fuchs. Handling complex boundaries on a cartesian grid using surface singularities. *International Journal for Numerical Methods in Fluids*, 35:125–150, 2001.

[105] A. Cesur and J. Revstedt. Vortex induced vibrations of multiple cylinders. *Proceedings of the Twenty Second Nordic Seminar on Computational Mechanics*, 2009. ISSN 1901-7278, DCE technical memorandum No. 11.

[106] A. Cesur and J. Revstedt. Influence of staggering on wake dynamics of multiple cylinders. *IUTAM Symposium on Bluff Body Wakes and Vortex-Induced Vibrations (BBVIV-6)*, 2010.

[107] G. Berkooz, P. Holmes, and J.L. Lumley. The proper orthogonal decomposition in the analysis of turbulent flows. *Annual Review of Fluid Mechanics*, 25:539–575, 1993.

[108] T.R. Smith, J. Moehlis, and P. Holmes. Low-dimensional modelling of turbulence using the proper orthogonal decomposition: A tutorial. *Nonlinear Dynamics*, 41:275–307, 2005.

[109] L. Sirovich. Turbulence and the dynamics of coherent structures. part1: coherent structures. *Quarterly of Applied Mathematics*, 41(XLV(3)):561–571, 1987.

[110] P.J. Schmid. Dynamic mode decomposition of numerical and experimental data. *Journal of Fluid Mechanics*, 656:5–28, 2010.

[111] C.W. Rowley, I. Mezić, S. Bagheri, P. Schlatter, and D.S. Henningson. Spectral analysis of nonlinear flows. *Journal of Fluid Mechanics*, 641:115–127, 2009.

[112] A. Ruhe. Rational krylov sequence methods for eigenvalue computation. *Linear Algebra and its Applications*, 58:269–295, 1984.